INT. J. REMOTE SENSING, 2001, VOL. 22, NO. 7, 1191–1234

Multifractals and resolution-independent remote sensing algorithms: the example of ocean colour

S. LOVEJOY†, D. SCHERTZER‡, Y. TESSIER† and H. GAONAC'H§

†Physics Department and GIROQ, McGill University, 3600 University St Montréal, Quebec, H3A 2T8, Canada
‡Laboratoire de Modèlisation en Mécanique, BP 162, Université de Pierre et Marie Curie, 4 Place Jussieu, Paris 75005, France
§GEOTOP, Université du Québec à Montréal, CP 8888, Succursale Centre-Ville, Montréal, Quebec, H3C 3P8, Canada

(*Received 19 March 1998; in final form 9 August 1999*)

Abstract. We argue that geophysical and geographical fields are generally characterised by wide range scaling implying systematic, strong (power law) resolution dependencies when they are remotely sensed. The corresponding geometric structures are fractal sets; the corresponding fields are multifractals. Mathematically, multifractals are measures that are singular with respect to the standard Lebesgue measures; therefore, they are outside the scope of many of the methods of classical geostatistics. Because the resolution of a measurement is generally (due to technical constraints) much larger than the inner scale of the variability/scaling, the observations will be fundamentally observer dependent; hence, standard remote sensing algorithms that do not explicitly take this dependence into account will depend on subjective resolution-dependent parameters. We argue that, on the contrary, the resolution dependence must be systematically removed so that scale-invariant algorithms independent of the observer can be produced. We illustrate these ideas in various ways with the help of eight-channel, 7 m resolution remote ocean colour data (from the MIES II sensor) over the St Lawrence estuary. First, we show that the data is indeed multiscaling over nearly four orders of magnitude in scale, and we quantify this using universal multifractal parameters. With the help of conditional multifractal statistics, we then show how to use multifractals in various practical ways such as for extrapolating from one resolution to another or from one location to another, or to correcting biases introduced when studying extreme, rare phenomena. We also show how the scaling interrelationship of surrogate and *in situ* data can be handled using vector multifractals and examine the resolution dependence of principle components in dual wavelength analyses. Finally, we indicate why the standard ocean colour algorithms have hidden resolution dependencies, and we show how they can (at least in principle) be removed.

1. Introduction

In the last 10 years, various technological developments have contributed to a profound change in many areas of remote sensing. New generations of satellites and airborne sensors with finer and finer space/time resolutions and more and more channels routinely supply digital data at rates greater than 1 Gb day^{-1}. At the same

International Journal of Remote Sensing
ISSN 0143-1161 print/ISSN 1366-5901 online
http://www.tandf.co.uk/journals

time, inexpensive high-resolution colour monitors, powerful computers and sophisticated software have opened up unprecedented opportunities for applications. Scientists using remotely sensed geophysical or geographical information are now daily faced with data spanning three (or more) of the roughly ten or so orders of magnitude of scale over which geophysical and geographical variability occurs[1]. Resolution (even if narrowly viewed as the purely technical problem of aggregating, sampling, archiving, intercomparing, and/or mapping) has become an operational consideration fundamental for the exploitation of the data.

Remote sensing resolutions are primarily fixed by technological constraints; the latter being typically at far larger spatial scales (smaller scale ratios) than the homogeneity scale which can readily be of the order of millimetres. In addition, virtually without exception, the radiances are non-linearly and non-trivially related to the physical processes of interest; in general neither the radiances themselves nor the corresponding sensor resolutions have any intrinsic geophysical/geographical significance *per se*. On the contrary, applications require that the radiances be transformed into surrogates for a wide variety of geophysical quantities. These are obtained as the outcome of often complex (and *ad hoc*) algorithms (themselves calibrated by *in situ* measurements) that are characterised by quite different space/time resolutions. Although it is rarely explicitly stated, remote sensing algorithms singularise the essentially arbitrary sensor resolution; when the algorithms are given some physical justification in terms of subpixel processes, the tacit assumption is that the subpixel fields are nearly homogeneous. However, when the sensor resolution improves, smaller and smaller structures and variability are discovered. A frequent consequence is that, when the old algorithms (calibrated with the old lower-resolution data) are applied to the new data, the results are initially *worse* not better[2] improvements only occur after new 'calibration'/'ground truth' experiments have provided the algorithms with new empirical coefficients.

While mainstream remote sensing approaches do acknowledge the resolution issue, theorising it as the Modified Areal Unit Problem (MAUP, Openshaw (1984)), an 'aggregation' or 'scaling up problem' (Bian 1997), the 'ecological fallacy' (Clarke and Avery 1976) or an 'optimum resolution' problem (Marceau *et al.* 1994a, b), implementations of these conventional approaches have typically only been attempted over less than a single order of magnitude of scale. For example, standard 'texture' analyses are based on only a factor three of coarse graining (e.g. Gonzalez and Wintz 1987). Implicit is the idea that, for every factor of three of so in scale, there are qualitative changes in the statistical properties of the fields, so that further extrapolation in scale is not warranted. However, since the 1980s, there has been an explosion in scale-invariant ideas: first fractals, then multifactals. In particular, with the development of generalized scale invariance (Lovejoy and Schertzer 1985, Schertzer and Lovejoy 1985, 1987, 1989a, b, Lewis *et al.* 1999), scale invariance can now be seen as a very general (non-classical) symmetry principle which *a priori* we may *expect* to be respected by complex non-linear dynamical systems with many

[1]For example, in the atmosphere, we have the ratio planet scale/dissipation scale $\approx 10^7$ m/10^{-3} m$\approx 10^{10}$. See Lovejoy *et al.*, (1993, 1997) and Sachs *et al.* (2000).

[2]One symptom of this is the finding by Chou (1991) that even the sign of the autocorrelations can change with resolution. In section 3.3, we show that scaling predicts that such sign changes can occur between different fields such as between remotely sensed surrogates and the corresponding *in situ* measurements.

degrees of freedom[3]. In other words, wide range scaling of geophysical and geographical processes (and their non-linearly related radiation fields) are expected with few, if any, breaks over wide ranges. Indeed, over 20 geophysical fields significant to remote sensing have been shown to be scaling over various ranges of scale: these include radar rain and ice surfaces, visible, infrared and passive microwave cloud and land reflectivities, topography, aeromagnetic and other fields (see Gabriel *et al.* (1988) and Lovejoy and Schertzer (1990) and the reviews Lovejoy and Schertzer (1993) and (1995)). Their resolution dependence in space and/or time has been quantified clearly demonstrating their systematic strong (power law) resolution dependencies. It should be mentioned that, perhaps due to the rapid pace of development of precise scaling notions, especially in physics, in recent years there has been an unfortunate tendency to use the same term but in a quite vague sense to denote nothing more than the general problem of changing resolution (see, for example, the special issue of the *International Journal of Remote Sensing*, **15**, entitled 'Scaling in Remote Sensing' which is largely of this genre).

Capitalising on these developments in scaling, various attempts have been made, starting in the 1980s, to develop scaling approaches capable of tackling resolution effects over wide rather than just narrow ranges of scale. Early attempts to exploit wide range scaling were based around the insight that geographical datasets (the most famous being the coast Brittany (Perrin 1913) and Britain (Richardson 1961, Mandelbrot 1967)) had tangents and lengths, respectively, that were purely resolution (and, hence, observer) dependent. However, if these sets are fractal, their fractal dimensions are objective (observer independent, scale invariant) measures of coastal irregularity. Early applications of scaling, therefore, transformed the two-dimensional remotely sensed fields into surfaces in three-dimensional (horizontal-intensity) spaces and treated the surfaces as fractal sets (Peleg *et al.* 1984, Pentland 1984, Ait-Kheddache and Rajala 1988, Keller *et al.* 1989, Mussigman 1990, Kuklinski 1994, Verge and Souriau 1994, Datcu and Seidel 1995, de Jong 1995, Rees 1995), with the hypothesis that different texture/irregularity corresponds to different fractal dimensions. A typical application was the use of 'local' fractal dimensions for image segmentation (e.g. Pentland 1984). This recognition that texture was inherently a scaling concept involving much wider ranges of scale than the usual factors of three was indeed a significant advance.

Although the use of fractal geometry represents a major step forward when compared with the classical non-scaling/scale-bound approaches, it still suffers from two basic limitations. The first is that (unlike scale-invariant geometric sets), scale-invariant fields are generally multifractal (not monofractal) and, hence, require an infinite number of exponents for their characterisation: a single fractal dimension is quite inadequate. This inadequacy is clearly shown in the analysis of visible ocean reflectivities shown in figure 1 (discussed in more detail in section 2). This figure shows that, while each visible brightness threshold does indeed accurately define a fractal set, the dimension of the latter depends crucially on the threshold. As the threshold is varied from dimmest to brightest values, the dimension of the exceedance sets varies from 2 to 0, which is the entire range available for sets embedded in two-dimensional space. The second limitation of the standard fractal approach is that,

[3]This attitude is the same as that adopted for the more familiar symmetries such as conservation of energy or momentum. Until we identify specific sources or sinks (corresponding to breaks in the underlying symmetries), we assume them to be conserved.

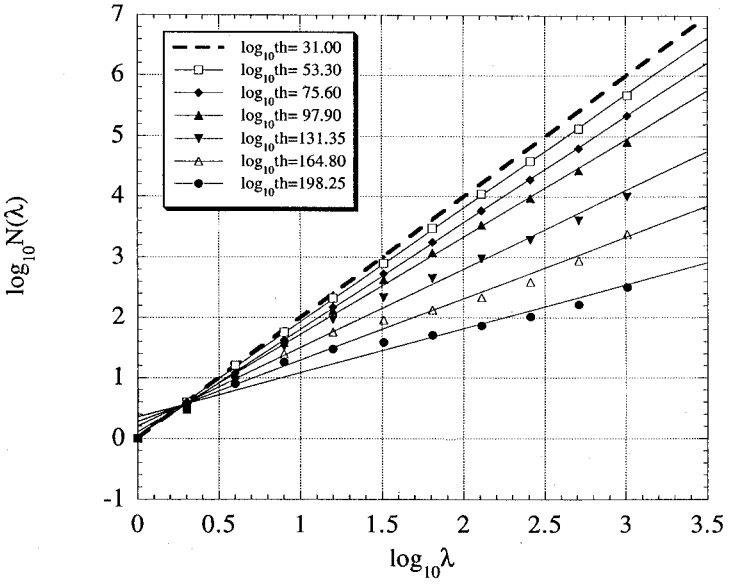

Figure 1. The results of functional box-counting of a 1024×1024 section of channel 2 data showing the number of boxes $N_T(\lambda)$ needed to cover the regions exceeding various brightness thresholds (T) ranging from values 31 to 198 (the data were 8 bit). Scaling predicts $N_T(\lambda) \approx \lambda^{D(T)}$, where λ = ratio of picture size to box size. Note that the fractional coverage (= probability of exceeding T) $= N_T(\lambda)/\lambda^2 = \lambda^{-c(T)}$, where $c(T) = 2 - D(T)$ is the co-dimension of the exceedance region. This figure shows that, no matter what exceedance threshold is used to define patches, the areas and fractioal coverage will depend strongly on resolution λ.

even for monofractals fields, simulations and analyses using generalized scale invariance (anisotropic scaling, see Pecknold *et al.* (1993) and (1999) for numerical simulations and Pflug *et al.* (1993) and Lewis *et al.* (1999)) show that what is perceived as texture is often more related to the type of scaling anisotropy, rather than to the completely seperate family of scaling exponents associated with statistical scaling exponents such as the fractal dimensions[4]. In contrast, the usual scaling approaches (this comment applies to many multifractal approaches as well), usually assume (at least implicitly) that the scaling is isotropic, i.e. that we have *self-similar* monofractals or *self-similar* multifractals.

Before continuing, let us emphasize the significance of the multifractality graphically exhibited in figure 1. Recall that the standard approaches (which purport to be very general) are, in fact, all based on various restrictive regularity/homogeneity type assumptions. For example, Raffy (1994b) developed a sophisticated mathematical framework for handling non-linear sensor averaging based on the assumption that remotely sensed fields can be considered as mathematical measures, correctly arguing that this has advantages over certain other approaches that involve restrictive assumptions about differentiability. So far, so good. However, without explicitly

[4]A scale-invariant system involves two mathematical groups and corresponding generators: the first determines the scale changing operator, i.e. it defines the (generally anisotropic, non-Euclidean) notion of scale; while the second determines the probability distributions at all scales. See Schertzer and Lovejoy (1987).

saying so, he then goes on to assume that the relevant measures are *regular with respect to the usual Lebesgue measures*! However, figure 1 already shows that every single intensity level (at least over the range of 10^3 accessible in the figure) are, on the contrary, *singular with respect to Lebesgue measures* requiring instead *singular multifractal measures*. Indeed, as far as we can tell from the figure, the fractal dimensions of all the exceedance sets are <2 for the two-dimensional image analysed; none of the slopes have the value 2 as implicitly assumed by Raffy (i.e. none of the *areas* converge to any well-defined limit over the observed range). Ironically, in the same paper, Raffy claims that his approach makes no 'a priori assumption on the measured parameter with respect to change of scale, as is made for example with the fractal assumption'! This is ironic, since certainly the multifractal assumption[5] (which, for example, allows for any slopes in figure 1 in the interval $[0,2]$) is more general than his (implicit) regularity assumption. However, so apparently 'natural' is this regularity assumption that the introduction to the special issue of *International Journal of Remote Sensing* (Raffy 1994a) on 'change of scale theory' doesn't even mention the word fractal' even though the entire point of the concept is to handle changes of scale over wide ranges! The term is also strangely absent from a recent review paper on the subject of scale in remote sensing (Cracknell 1998), nor does it appear in a recent paper on the nature of the 'pixel' (Fisher 1997) which is otherwise critical of the standard approach.

We have mentioned that, in the early 1980s, it was realised that the appropriate framework for scale-invariant fields was multifractals, that fractals were only adequate for handling geometric sets of points. It is perhaps not surprising, therefore, that remote sensing supplied the data for the very first empirical multifractal analyses, that of radar reflectivities of rain (Schertzer and Lovejoy 1985, Lovejoy *et al.* 1987, Lovejoy and Schertzer 1988); since then, many have followed. Multifractal analyses using remotely sensed data now include microwave backscatter from ice (Falco *et al.* 1996), visible, infrared and microwave radiances from clouds (Gabriel *et al.* 1988, Lovejoy and Schertzer 1990, Lavallée *et al.* 1993a, Tessier 1993, Davis *et al.* 1996), ocean surfaces (Tessier *et al.* 1993) and surfaces in the visible and infrared from volcanoes (Gaonac'h *et al.* 2000, Harvey *et al.* 2000, Laferrière and Gaonac'h 1999). These and other studies have laid the empirical basis for the direct use of multifractal modelling of matter–radiation interactions in order to quantitatively interpret remotely sensed data, to relate visible radiative transfer to fractal and multifractal cloud liquid water densities (Davis *et al.* 1990, 1993, Gabriel *et al.* 1990, Lovejoy *et al.* 1990, 1995, 1997, Naud *et al.* 1996) and to relate microwave reflection to multifractal scatterer distributions[6] (Lovejoy *et al.* 1996). Indeed, such explicit use of multifractal modelling promises to allow a fundamental physical understanding of the extreme variability of many remote datasets.

We have argued that the great promise of the multifractal approach is precisely to exploit the observed wide range scaling of the underlying geophysical/geographical fields to overcome the problem of resolution dependency altogether. This wide range scaling approach is currently gaining ground, as witnessed, for example, in the recent workshop on 'Resolution dependence and multifractals in remote sensing and

[5] In his text, it is not clear to exactly what 'fractal assumption' he was referring.

[6] We might also mention the use of fractal surfaces to model bidirectional reflectance functions (Rees 1995).

geographical information systems' (McGill University[7], 10–12 June 1996). Therefore, it is somewhat paradoxical that there has recently arisen another quite different multifractal approach to remote sensing which denies (or, more precisely, is agnostic) about the very existence of any scaling properties whatsoever! For example, Mignot *et al.* (1992), Lèvy-Vèhel and Berroir (1994), Bourissou *et al.* (1994), Lèvy-Vehel and Mignot (1994) and Lévy-Vehel (1995) purport to use multifractal techniques for analysing remotely sensed images but without making any assumptions about the scale invariance of the latter. In effect, they argue that, even without this basic property, multifractal techniques might still be useful. This attitude is consistent with the fact that they typically apply their techniques only over the same narrow ranges as the standard techniques (cf. factors of three in scale ratio in Lévy-Vehel (1995)); indeed, due to this limitation, such techniques are hard to distinguish from standard segmentation and texture analysis.

In this paper, we argue that the existence of scaling resolution dependence over wide ranges of scale not only allows, but also demands, the development of qualitatively new remote sensing algorithms. Rather than being based on unrealistic subpixel homogeneity assumptions requiring subjective resolution-dependent calibration at the arbitrary sensor resolution scale, these methods directly exploit the scaling and can provide algorithms that are independent of the sensor and *in situ* calibration resolutions. These scale-invariant remote sensing algorithms are based on the scale/observer-independent exponents that determine how the statistics change with resolution, rather than the value of the fields at any particular (subjective) scale. Early examples of such algorithms are Schmitt *et al.* (1997), Martinez (1998) and Harvey *et al.* (1999). Here, we illustrate our approach with the example of the remote sensing of phytoplankton.

Although the paper is based around the important remote sensing problem of ocean colour, its main aim is to demonstrate the power and scope of the scale-invariant approach and the concomittant necessity of developing resolution-independent algorithms so as to entirely remove the subjective (observer) dependence in the existing approaches. Section 2, therefore, provides a brief overview of the relevant properties of multifractals and the corresponding multifractal analysis techniques. Using the eight-channel, 7 m MIES II sensor, we quantify the multiscaling of the visible radiances over an unprecedented four orders of magnitude in scale. Section 3 gives various examples of the ways that multifractals can be used to resolve resolution problems; we concentrate on the related problems of changing resolution for a given field (i.e. of extrapolating from large to small scales or visa versa), of extraplolating data from one location to another (a component of multifractal objective analysis), on biases introduced by conditional sampling, and, finally, the use of scaling surrogate data indicating the pitfalls of the standard fixed-resolution cross-correlation analysis. In section 4, we come back to the ocean colour problem, showing how the standard algorithm for determining chlorphyll-like pigment from the Coastal Zone Colour Scanner (CZCS) can be modifed to render it scale invariant. In section 5, we conclude.

2. Phytoplankton and remotely sensed ocean colour

2.1. *Scaling and phytoplankton patchiness*

One of the main difficulties in mapping phytoplankton or in estimating their abundance (or biomass) is that it forms 'patches' of all sizes and that these structures

[7]Organized jointly with the Canadian Centre for Remote Sensing, there were roughly 75 participants.

are not static but evolve in time. An early scaling theory of this patchiness is due to Denman and Platt (1975), Denman *et al.* (1976), Platt (1978) and Platt and Denman (1975), who used a turbulence framework to show that the energy spectrum had the scaling form $E(k) \approx k^{-\beta}$ (k is a horizontal wavenumber). By arguing that patch lifetimes were growth dominated, they found theoretically that the chlorophyll fluctuation spectrum had $\beta = 1$. Since then (while generally agreeing about the scaling) a series of *in situ* fluorescence (phytoplankton surrogate) measurements have been inconclusive about the empirical value of the exponent; some coming close to the Denmann–Platt value 1, while others are closer to $\beta \approx 5/3$, the value expected for a passive scalar advected by turbulence. More recently, Pascual *et al.* (1995) showed that, in time, over long periods (days to months), fluctuations in the related zooplankton patchiness were multifractal, not monofractal; hence, the scaling exponent is just one in the infinite hierarchy of exponents necessary to specify the statistics[8]. Other temporal analyses (at much smaller time scales (0.5 s to 11 h), Seuront *et al.* (1996a, b) have shown that, while the high frequencies (> 0.04 Hz) can be passive scalar-like, the low frequencies are, in fact, 'in between', with $\beta \approx 1.22$. Claeredeboudt *et al.* (2000) and Lovejoy *et al.* (2000), using spatial phytoplankton data, show that the large scales ($\geqslant 100$ m) were indeed in between ($\beta \approx 1.18$, in agreement with Seuront *et al.* (1996)), but with more (rather than less) high-frequency variability ($\beta \approx 0.4$ rather than $\beta \approx 1.75$; see table 2). They hypothesised that the low frequency is a combined turbulence/growth-dominated regime (rather than only a growth-dominated regime), while the small scale is a regime dominated by predator/prey (zooplankton/phytoplankton). All these multifractal studies found that the plankton density is of the universal multifractal type (see below), and they found mutually consistent estimates of the three universal multifractal parameters for the phytoplankton surrogate[9].

2.2. *Ocean colour as determined by remote sensing*

Because of the severe practical limitations of *in situ* plankton mapping (even with the fluorescence surrogate), it is important to use other surrogates that can be easily sensed remotely. At present, the main technique is to use the fact that chlorophyll has pigment with well-defined absorption characteristics so that the concentration of phytoplankton is linked to 'ocean colour'. The standard method of estimating the phytoplankton density from ocean colour is to relate radiances in bands near 443 nm (sensitive to chlorophyll) to those in the red (insensitive, typically near 550 nm); the relative reflectivities (at the available resolution) defines the 'colour'. After removal of atmospheric corrections, the usual approaches compare remote measurements of these reflectivities with *in situ* chlorphyll-like pigment concentration measurements and relate the two via *ad hoc* regression schemes. The main shortcoming of this approach is that, at best, algorithms have been devised at single (subjective) remote sensor resolution scales (often of the order of a kilometre; cf. the CZCS, see below) using calibration by a single (different) subjective *in situ* scale typically of the order of metres (still much larger than the internal scale of homogeneity). In order to objectively characterise the chlorophyll-like pigment concentrations, a scale-invariant algorithm (for example, based on a scale-invariant notion of ocean colour) is necessary. In section 4, we discuss this in more detail; first, we examine the statistical

[8] Unfortunately, they calculated neither spectra nor structure functions so that we cannot estimate their exponent β.

[9] The only exception is Pascual *et al.* (1995), who made no attempt to check this.

properties of the raw remotely sensed radiances scale by scale and intensity by intensity.

In order to illustrate our ideas, we now analyse ocean reflectances, determining their ranges and types of scaling. The data were collected by aircraft with the multi-detector electro-optical imaging scanner II (MEIS II) sensor on 3 September 1991, from Trois-Pistoles to Montmagny along the St Lawrence river (figures 2 and 3). There were two flight lines, one predominantly over land and the other over water. Only the data over water were analysed. The sample used is 1024×26937 pixels, and eight frequency bands were recorded (from 433 to 900 nm; see table 1). The central wavelengthes of five of these channels were close to the wavelengths of the CZCS sensor.

2.3. *The scaling range*

Perhaps the most sensitive method of detecting scaling and determining its limits is the power spectrum. We calculated this using the first 2^{14} points in the swath, averaging the one-dimensional spectra over the 2^{10} cross range tracks[10]. The spectra for the different channels are shown in figure 4(*a*). For channels 2, 3, 5, 6 and, especially, channel 7 (which is the most sensitive to chlorophyll[11]), there is a break in the scaling at roughly 100 m. This is roughly the same scale as the 'planktonoscale' at which Claeredeboudt *et al.* (2000) and Lovejoy *et al.* (2000) observed a scaling break with *in situ* chlorophyll fluorescence measurements (see figure 4 (*b*). This break,

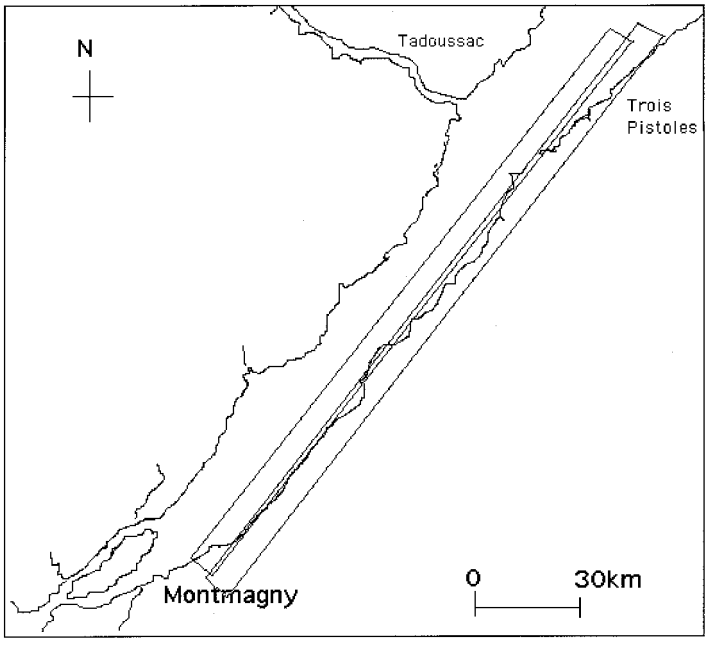

Figure 2. Flight path of the aircraft recording the MEIS II data.

[10]We did not calculate the two-dimensional power spectrum because this would require the use of square samples and would have thus limited our range of scales to 2^{10}.

[11]For brevity, we will use the expression 'chlorophyll' instead of the more precise term 'chlorphyll-like pigment'.

however, is absent in channels 4 and 8, the latter being the least chlorophyll-sensitive band. With this exception, we can see that the scaling is extremely good over all the available range, i.e. from[12] 14 m to 7×2^{14} m ($\approx$ 110 km), for the other channels; it is the longest range scaling analysis of any remotely sensed data of which we are aware. The spectral slopes are nearly the same for all channels in the range of 100 m–110 km, i.e. they vary from 1.24 to 1.26, which is very close to the value 1.22 found in Seuront *et al.* (1996) and Lovejoy *et al.* (2000) (see figure 4(*b*), table 2[13]). We believe that both the remote and *in situ* scaling breaks share a common origin and that the scale of this break is important in evaluating the pigment concentration from remotely sensed data.

The spectral slopes are nearly the same for all channels in the scaling range (they vary from $\beta\approx 1.24$ to $\beta\approx 1.26$; cf. $\beta\approx 1.18$ for the *in situ* fluorescence). At the high frequencies, the chlorophyll-sensitive channel 7 also follows more or less the high-frequency *in situ* spectra. Although, due to its narrow range (factor of $\approx 100/14 \approx 7$), the accuracy is not high, we obtain $\beta\approx 0.3$, which is close to the high-frequency *in situ* fluorescence value ($\beta\approx 0.4$, table 2).

2.4. *The type of scaling: multifractals and universal multifractals*

If the radiances were monofractal (e.g. if they were scaling but quasi-gaussian), then, at least for isotropic scaling, the basic scaling properties would be determined by the spectral exponent β. However, theoretically we have seen that this is generally not the case, and figure 1 shows explicitly for the data analysed here that the fractal dimension is not constant but varies systematically as a function of the reflectivity threshold (T). While the functional box-counting (Lovejoy *et al.* 1987) shown in figure 1 is simple and shows graphically how the fractional coverage by various patch densities varies as a function of the scale and threshold, it is still not completely observer independent, since the threshold is defined by an arbitrary subjective (7 m) resolution. Therefore, the dimension as a function of threshold itself is not an objective function of the ocean surface; we must express the latter in terms of scale-invariant singularity values[14] $\gamma = \log T/\log \lambda$. The multifractal properties can be investigated by two equivalent routes: the probability distribution and the statistical moments. Considering first the probability distributions (Schertzer and Lovejoy 1987),

$$\Pr(\phi_\lambda \geqslant \lambda^\gamma) \approx \lambda^{-c(\gamma)} \tag{1}$$

$\lambda = L/\ell$, where L is the largest scale of interest and ℓ is the resolution of the observation, γ is the order of singularity, $c(\gamma)$ is the co-dimension function of the singularities and ϕ_λ is the conserved field (see below) at resolution λ. The equality '$\approx$' means to within constant or slowly varying factors (such as $\log \lambda$). Similarly, the statistical moments are given by

$$\langle \phi_\lambda^q \rangle = \lambda^{K(q)}, \quad \lambda > 1 \tag{2}$$

[12]The Nyquist wavelength is $2\times 7 = 14$ m.

[13]Since the measurements were not performed during the blooming season, we could not substantiate the existence of bloom related breaks. See Barale and Schlittenhardt (1993) and references therein.

[14]Note that, in this equation, T must be appropriately normalized/nondimensionalized by the ensemble average at the largest scale.

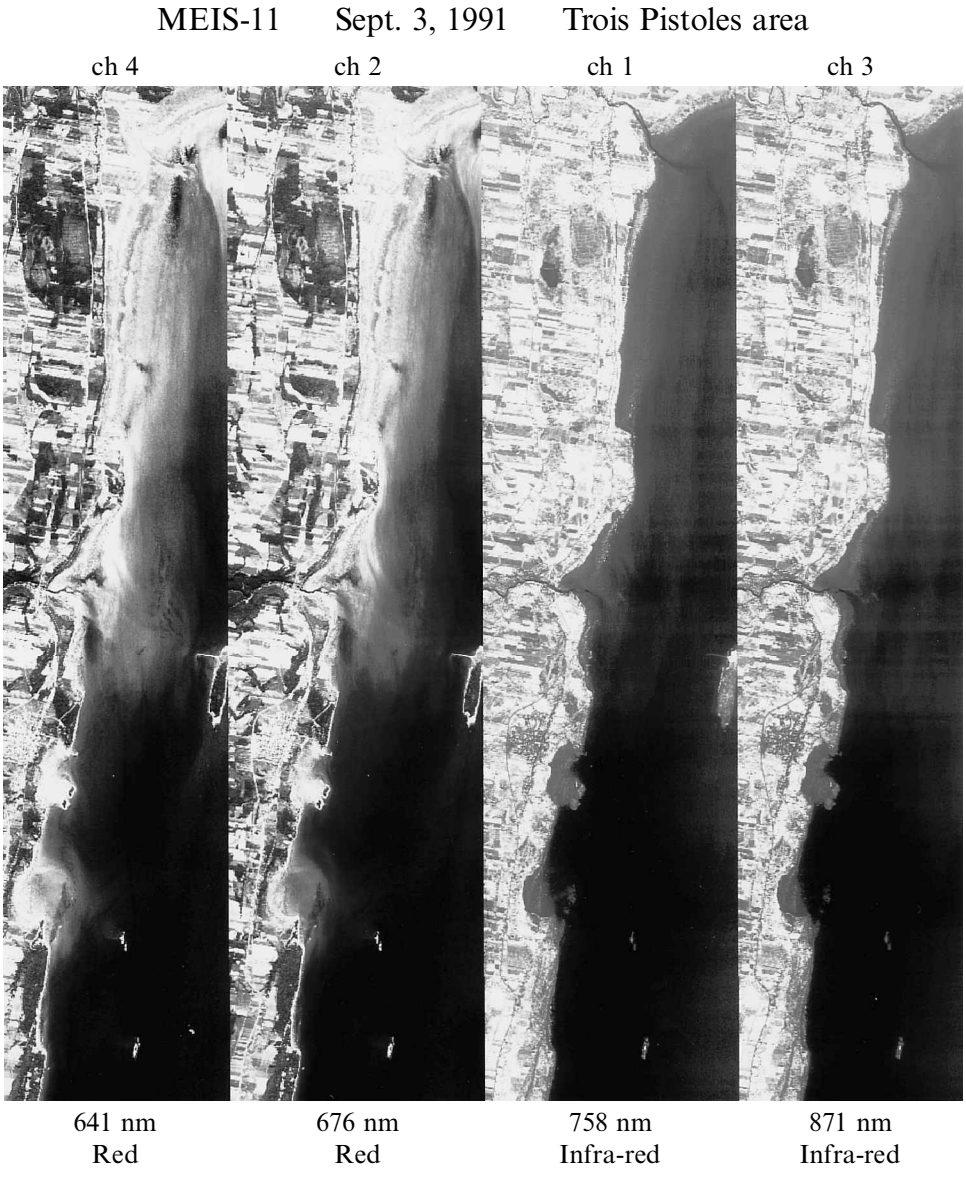

Figure 3. A small sample of the land dominated run, showing both land and ocean for the various channels.

where $K(q)$ is the multiple scaling exponent for moments; the two are related to each other via a Legendre transform (Parisi and Frisch 1985):

$$c(\gamma) = \max_q (q\gamma - K(q))$$
$$K(q) = \max_\gamma (q\gamma - c(\gamma)) \tag{3}$$

The only restriction on $c(\gamma)$ and $K(q)$ is that they are convex. In actual dynamical

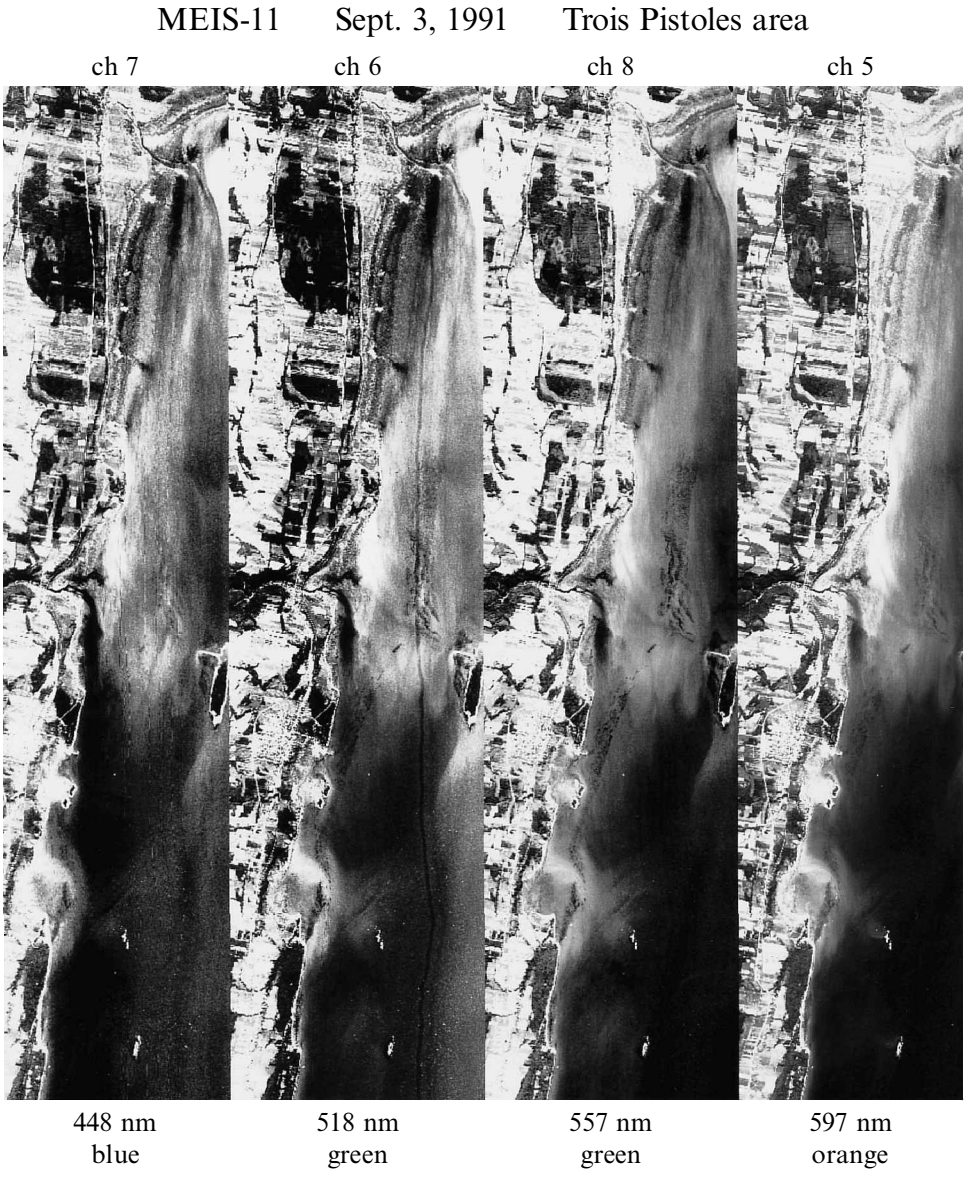

systems involving non-linear interactions over a continuum of scales (and/or involving multiplicative 'mixing' of different processes), we generally obtain a considerable simplification. Schertzer and Lovejoy (1987) and Schertzer *et al.* (1991) showed that cascade processes possess stable (attractive) universal generators irrespective of the details of the dynamics (see also Brax and Pechanski (1991) and Kida (1991) and, for a recent debate, Schertzer and Lovejoy (1997)). Recently, it has been suggested that a weaker form of universality involving log-Poisson distribution might also be relevant (e.g. She and Levesque 1994); however, it is not stable/attractive nor is it well supported by the turbulence data (Schertzer *et al.* 1995, 1997) that provided its initial motivation.

Table 1. The various multifractal parameters estimated for one-dimensional strip of MEIS II data.

Channel	Wavelength	β	α	C_1	H
1 (infrared)	758	1.26	1.98	0.05	0.18
2 (red)	676	1.24	2.01	0.06	0.18
3 (infrared)	871	1.26	2.03	0.06	0.19
4 (red)	641	1.25	1.97	0.05	0.17
5 (orange)	597	1.26	2.05	0.06	0.19
6 (green)	518	1.24	1.98	0.05	0.17
7 (blue)	448	1.26	2.00	0.06	0.19
8 (green)	557	1.26	1.95	0.04	0.17
Average		1.25	1.99	0.05	0.18

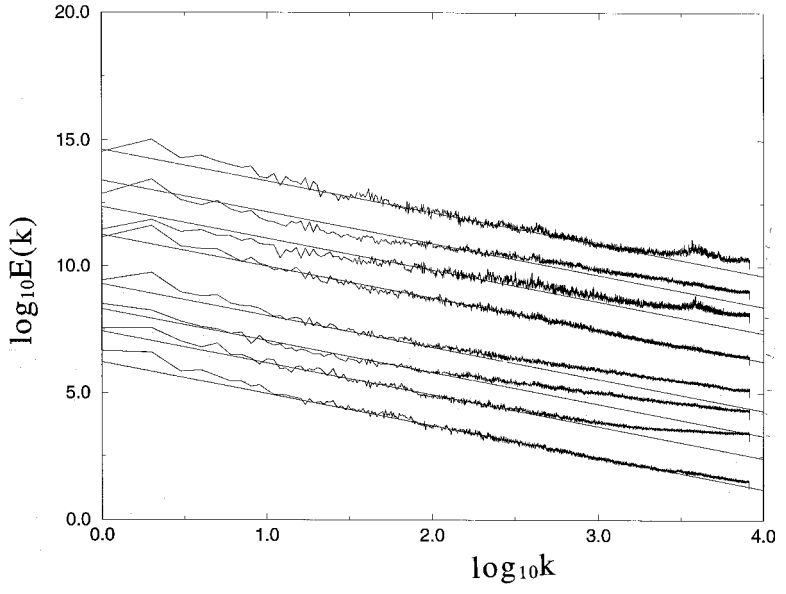

Figure 4(*a*). Power spectrum for all eight channels recorded, channels 1 to 8 from bottom to top. The reference line has a slope $\beta \approx 1.25$, close to the *in situ* value 1.18; see table 2.

The universal $K(q)$ functions for conservative processes are of the following forms:

$$K(q) = \begin{cases} \dfrac{C_1(q^\alpha - q)}{\alpha - 1} & \alpha \neq 1 \\ C_1 q \,\mathrm{Log}(q) & \alpha = 1 \end{cases} \tag{4a}$$

where $0 \leqslant \alpha \leqslant 2$ is the multifractal index, which quantifies the distance of the process from monofractality; $\alpha = 0$ is the monofractal β-model of turbulence (Novikov and Stewart 1964, Mandelbrot 1974, Frisch *et al.* 1978) and $\alpha = 2$ (the maximum) is the lognormal model. C_1 is the co-dimension of the mean of the process; it quantifies

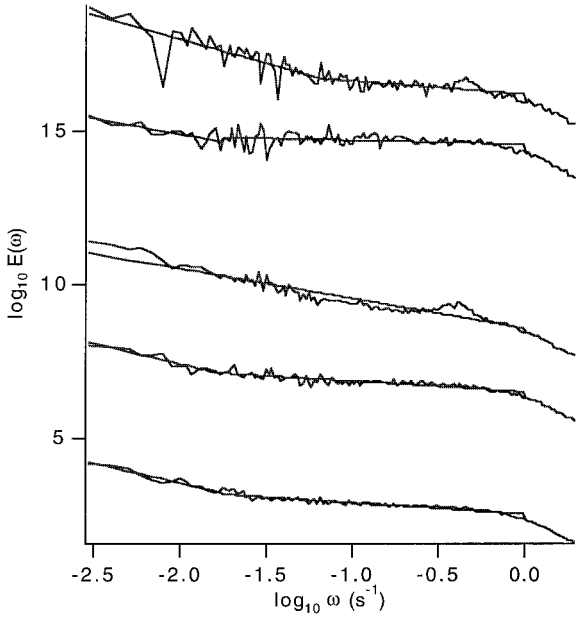

Figure 4(*b*). *In situ* fluorescence spectra from Lovejoy *et al.* (2000). The boat speed was 1.3 m/s.

Table 2. Fluorescence global comparisons. Part I refers to Claerdeboudt *et al.* (2000, part II to Lovejoy *et al.* (2000). For part II, the errors (parentheses) are interbay average variabilities. The low frequency C_1, α values were not estimated due to an inadequate range of scales.

	C_1	α	H	β
Low frequency				
Space: part I	—	—	0.21 (0.06)	1.31 (0.13)
Space: part II	—	—	0.11 (0.05)	1.18 (0.1)
Time: Seuront *et al.* (1996a)	0.02 (0.01)	0.8 (0.02)	0.12	1.22
High frequency				
Space: part I	0.064 (0.05)	1.84 (0.01)	− 0.31 (0.02)	0.26 (0.03)
Space: part II	0.022 (0.01)	1.86 (0.10)	− 0.27 (0.05)	0.41 (0.1)
Time: Seuront *et al.* (1996a)	0.04 (0.01)	1.80 (0.05)	0.41	1.75
Time: Seuront *et al.* (1996b)	0.035	1.80	0.36	1.66

the sparseness of the field values which give a dominant contribution to the mean. The corresponding $c(\gamma)$ obtained by Legendre transform is

$$c(\gamma) = C_1 \left(\frac{\gamma}{C_1 \alpha'} + \frac{1}{\alpha} \right)^{\alpha'}; \quad \frac{1}{\alpha} + \frac{1}{\alpha'} = 1 \tag{4b}$$

In order to directly test the universality hypothesis, and to estimate α, C_1, we used the double trace moment (DTM) technique (Lavallée 1991, Lavallée *et al.* 1993b). The basic idea is to define a new exponent function $K(q, \eta)$ via the following equation:

$$\left\langle (\phi_\Lambda^q)_\lambda^q \right\rangle = \lambda^{K(q,\eta)} \tag{5}$$

This notation indicates that we take the various powers η of the field at its highest resolution scale ratio (Λ = image-size/pixel-size), then degrade the result to a lower (ϕ intermediate) resolution (λ) and finally (ensemble) average the qth power of the result.

The scaling exponent $K(q, \eta)$ is related to $K(q, 1) \equiv K(q)$ by

$$K(q, \eta) = K(q\eta, 1) - qK(\eta, 1) \tag{6a}$$

The advantage of the DTM over other techniques is that, in the case of universal multifractals, applying equation (6a) to the form in equation (4a), we find that $K(q, \eta)$ has a particularly simple dependence on η:

$$K(q, \eta) = \eta^{\alpha} K(q) \tag{6b}$$

Therefore, α can be estimated on a simple plot of $\log K(q, \eta)$ versus $\log\eta$ for fixed q.

The above applies to processes that are the direct result of a multiplicative cascade process in which some quantity (analogous to the energy flux in turbulent cascades) is conserved from scale to scale. However, *a priori*, there is no reason to expect the observed processes to be conserved; they will more generally be related to a conservative process by integrations of various (generally fractional) orders denoted H (differentiations are integrations of negative order and hence are obtained for $H < 0$; see Schertzer and Lovejoy (1987) and Naud *et al.* (1996)). This is the 'fractionally integrated flux' model. If the process is non-conserved, it suffices to perform the inverse fractional integration/differentiation so as to return it to the underlying conservative process. Since fractional integration of order H corresponds to power law filtering, this is conveniently done by Fourier methods. Alternatively, since in practice it suffices to differentiate by an amount at least $-H$ (Lavallée *et al.* 1993b), if $H < 1$, one can use a first-order derivative (roughly equivalent to filtering by the wavenumber modulus), which in turn can easily be approximated by using the (absolute) gradient of the series.

Once C_1, α have been estimated, one can calculate $K(2)$ for the conserved process (using equation (3) with $q = 2$) and then calculate H using the result of appendix A.2. The parameter H can then be estimated by

$$H = \frac{\beta - 1 + K(2)}{2} = \frac{\beta - 1}{2} + \frac{C_1(2^{\alpha} - 2)}{2(\alpha - 1)} \tag{7}$$

This technique was applied to the different strips which were fractionally integrated by filtering[15] by $k^{0.2}$. The moments for different values of q ($\eta = 1$) for channel 4 are shown in figure 5. As expected, the scaling is good for all moments. We also calculated the curves for $\log_{10} K(q, \eta)$ versus $\log_{10} \eta$ for all the different channels with $q = 0.5$ (figure 6). As we can see, there is very little dispersion in the various curves, so that $K(0.5, \eta)$ is nearly the same for all channels. In particular, the slope yields an estimate of α and the intercept of C_1 (cf. equation (6b) and use $C_1 = K(q)(\alpha - 1)/(q^{\alpha} - q)$ to calculate C_1 from the graphically determined $K(q, 1) = K(q)$). Note that the curvature at high values of η is due to the limited number of samples; this can be explained in terms of multifractal phase transitions which arise from finite sample size effects (possibly) combined with divergence of high order statistical moments[16] (Schertzer and Lovejoy 1994). The values of the estimated parameters α, C_1 and H are shown in table 1. As we can see, all three channels are roughly compatible with the same

[15] To avoid numerical problems in the fractional integration, standard windowing techniques should be used.

[16] In the former case, the transition is second order; in the latter, it is first order.

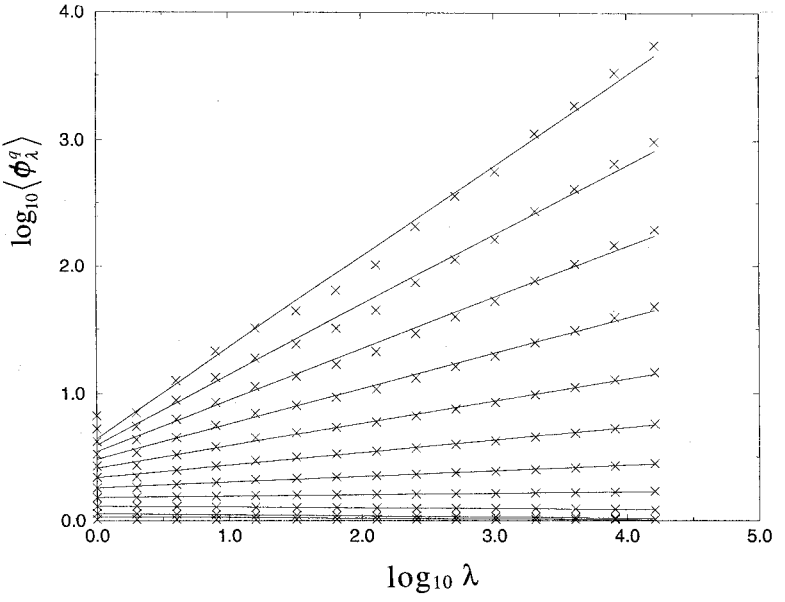

Figure 5. $\mathrm{Log}_{10}\langle\varphi^q\lambda\rangle$ versus $\log_{10}\lambda$ for values of q decreasing (top to bottom) from 8 to 0 in increments of 0.8. Note the excellent (multi) scaling over the entire range.

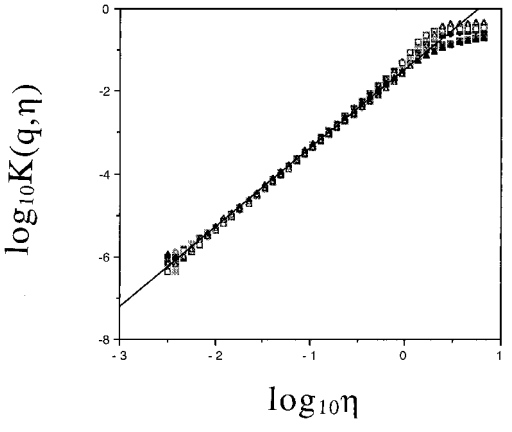

Figure 6. $\mathrm{Log}_{10}\ K(q,\eta)$ versus $\log_{10}\ \eta$ for all eight channels with $q=0.5$. The reference line has a slope $=1.9$.

value of the parameters, i.e. $\alpha=2.0\pm0.1$, $C_1=0.05\pm0.01$ and $H=0.18\pm0.01$. In Seuront *et al.* (1996a, b), Claerdebout *et al.* (2000) and Lovejoy *et al.* (2000), the multifractal parameters for *in situ* data were estimated (see table 2), and the values of the parameters α and C_1 of the remotely sensed images are the same (within statistical errors) as the *in situ* measured values. We also note that $\alpha=2$ is the maximum of the multifractal index and corresponds to a process with a log-normal generator[17].

[17]Note that, strictly speaking, DTM only determines the behaviour of $K(q)$ (with linear term removed) near $q=0$, i.e. its degree of nonanalyticity at the origin; the result $\alpha\approx2$, therefore, is compatible with any analytic $K(q)$; the log-normal multifractal is then simply the closest pure quadratic approximation.

2.5. *Extreme events, multifractal phase transitions and self-organised criticality*

We will now consider an important theoretical and empirical aspect of the data; the statistics of the extremes. For multifractal processes, the statistics of ϕ_λ resulting purely from dynamics at larger scales (smaller λ) are very different from those averaged at the same scale but whose dynamics continue to much smaller scales. The former are called the bare quantities and the latter the 'dressed' quantities[18]. The main difference between the two is that all the statistical moments of the bare field ϕ_λ converge as the sample size increases, whereas the moments of the dressed $\phi_{\lambda,d}$ will generally diverge[19] with sample size if q is large enough:

$$\langle \phi_{\lambda,d}^q \rangle \to \infty \; ; \; q \geqslant q_D \tag{8}$$

This divergence corresponds to hyperbolic fall-off the probability distribution, i.e.

$$\Pr(\phi_{\lambda,d} \geqslant s) \approx s^{-q_D} \; (s \gg 1) \tag{9}$$

The divergence of statistical moments and spatial scaling can be taken as the defining property of self-organised criticality (SOC; Bak *et al.* 1987, 1988) so that such (non-classical[20]) SOC is in fact a generic property of multifractal fields (Schertzer and Lovejoy 1994). Since finite samples will always yield finite moments, the divergence can be observed either via the divergence of empirical moments with increasing sample size or via discontinuities in the derivatives of the observed scaling exponents $K(q)$ and $c(\gamma)$. Since there is a formal analogy between multifractals and classical thermodynamics (Schuster 1988, Schertzer and Lovejoy 1994), these discontinuities result in 'multifractal phase transitions'.

The probability distribution for absolute intensity gradients Δi is shown for channel 8 in figure 7 (*a*) and for all channels in figure 7 (*b*). Channel 8 is shown seperately, since it has the most convincing power law tail with the value $q_D \approx 3.6$. Note that the very largest gradients have faster fall-off; these gradients (>100 digital counts in 8-bit data) are near the limit of the discretisation and could be caused by inadequate discretisation or related instrument response/saturation problems. In figure 7(*b*), the behaviour is not so clear, but there is general trend with roughly the same slope (see the reference lines with slope 3.6), and once again one may suspect instrumental problems at the extreme gradient end. The value $q_D \approx 3.6$ is close to the *in situ* value $q_D \approx 3$ reported in[21] Lovejoy *et al.* (2000). It is worth mentioning that large datasets are typically needed to estimate these exponents; the necessary size can be quantified with the notion of 'sampling moment' q_s (Schertzer and Lovejoy 1989b), which is the largest moment that can be reliably estimated for a given sample size and α, C_1 values. Here, we estimate $q_s \approx 4.5$, which is $> q_D$, so that we may conclude that our estimate of q_D is indeed based on an adequately large sample.

[18]This jargon was introduced into the multifractal literature by Schertzer and Lovejoy (1987) and is borrowed from renormalisation theory.

[19]Various multifractal processes can be constructed which have intrinsic maximum orders of singularity; in these processes, $q_D \to \infty$ for sufficiently large averaging dimension D; hence, in these 'conditionally hard' multifractal processes, the divergence can be avoided.

[20]Classical SOC is based on cellular automaton type models and are characterized by avalanche-like extreme events associated with the algebraic probability tails. It is restricted to zero-flux processes whereas multifractal SOC has the advantage of having finite flux.

[21]This *in situ* analysis suffered from similar instrumental problems; however, the *in situ* values of q_D for temperature, O_2 density, salinity and transmittivity were 4.3, 4.1 and 4.3, respectively.

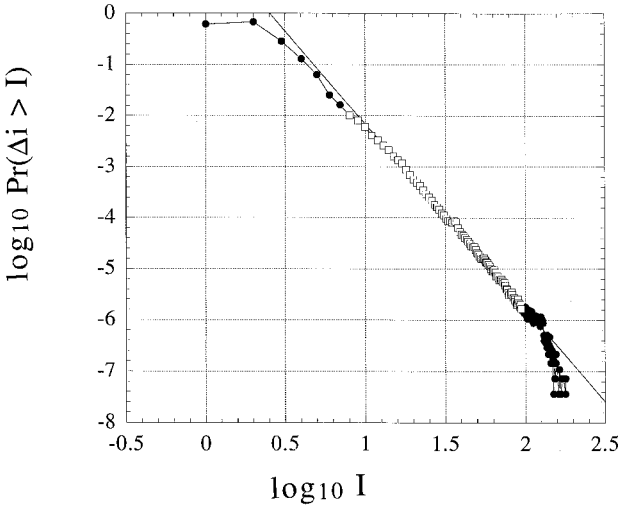

Figure 7(*a*). $\text{Log}_{10}\ \Pr(\Delta i > I)$ versus $\log_{10}\ I$ for channel 8. The reference line has a slope of -3.62 and was fit to the squares.

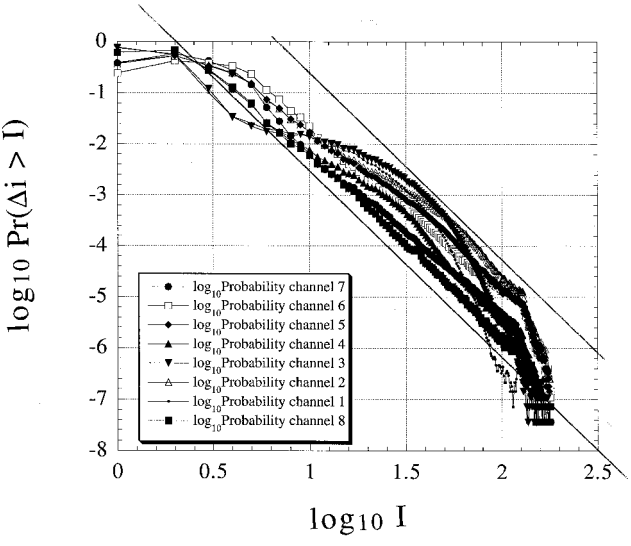

Figure 7(*b*). $\text{Log}_{10}\ \Pr(\Delta i > I)$ versus $\log_{10}\ I$ for all channels.

3. Conditional Multifractal statistics

3.1. *Using multifractals to extrapolate from one resolution to another*

Before considering the problem of comparing different data types at different resolutions (such as *in situ* and remote surrogates), we first consider the problem of changing resolution for data of a single type. We have seen that the appropriate scale-invariant (resolution-independent) characterisation of a multifractal is via the exponents γ, $c(\gamma)$, $K(q)$ (see figure 8(*a*) for a schematic). If we are only interested in comparing the unconditional statistics at different scales, then this is adequate. For example, we can use equation (1) and transform our resolution λ data ϕ_λ into singularities: $\gamma = \log \phi_\lambda / \log \lambda$ and then calculate the probability from the resolution-

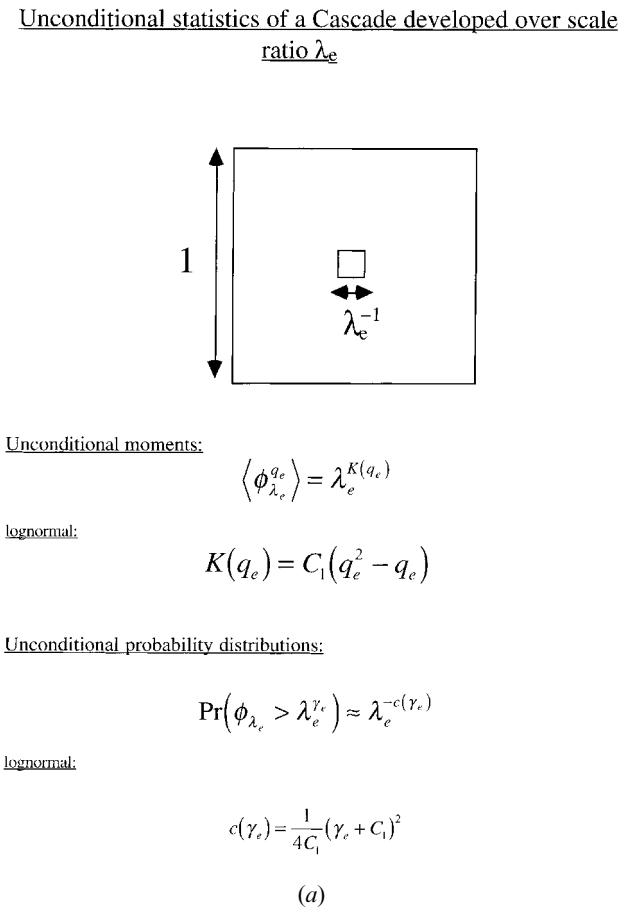

Figure 8. Schematic diagrams showing the various conditional statistics discussed in the text.

independent $c(\gamma)$. However, it is often of interest to use conditional information such as knowledge of the measured value ϕ_{λ_m} ($= \lambda_m^{\gamma_m}$, singularity γ_m, resolution λ_m, m for measured, e for extrapolated) and we wish to extrapolate to higher or lower resolutions λ_e either by determining the conditional probability distributions or the conditional expectations. In particular, the conditional expectation of ϕ_{λ_e} given ϕ_{λ_m} provides the statistically optimum estimator of ϕ_{λ_e}.

It turns out that, for technical reasons, the easiest way to calculate the conditional expectations, joint and conditional probability distributions is via the cross-moments; this is developed in appendix A (see also Salvadori *et al.* 2000 for a general statement of the conditioning problem). In order to calculate the conditional expectations from the cross-moments, first define the conditional probabilities $p(\gamma_e|\gamma_m)$ from the joint probabilities $p(\gamma_e, \gamma_m)$ of obtaining both estimated singularity γ_e and measured singularity γ_m:

$$p(\gamma_e|\gamma_m) = \frac{p(\gamma_e, \gamma_m)}{\int p(\gamma_e, \gamma_m)\, d\gamma_e} \tag{10}$$

Disaggregation: Downscaling:

(Measurement Scale Larger than the estimated scale)

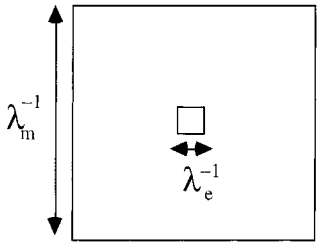

Conditional moments:

$$\left\langle \phi_{\lambda_e}^q \right\rangle_{\gamma_m} = \left(\frac{\lambda_e}{\lambda_m}\right)^{K(q)} \lambda_m^{q\gamma_m} = \lambda^{K(q)} \phi_{\lambda_e}^q ; \quad \lambda = \lambda_e / \lambda_m$$

Conditional probability distributions:

$$\Pr\left(\varphi_{\lambda_e} > \lambda_e^{\gamma_c} | \gamma_m\right) \approx \lambda_e^{-(1-\zeta)c\left(\frac{\gamma_c - \zeta\gamma_m}{1-\zeta}\right)}$$

$$\zeta = \frac{\log \lambda_m}{\log \lambda_e}$$

(*b*)

The conditional statistical moments are now given by

$$\left\langle \phi_{\lambda_e}^{q_e} \right\rangle_{\gamma_m} = e^{K(q_e|\gamma_m)} = \int \lambda_e^{q_e \gamma_e} p(\gamma_e | \gamma_m)\, d\gamma_e \tag{11}$$

(we use the *e*-based second characteristic functions K rather than the usual λ-based ones, since we are interested in using different resolutions for measurements and extrapolations). We now introduce the following definition of $K(q_e, \gamma)$:

$$e^{K(q_e, \gamma_m)} = \int e^{q_e \gamma_e \log \lambda_e} p(\gamma_e, \gamma_m)\, d\gamma_e \tag{12}$$

From equations (10–12), we have

$$K(q_e | \gamma_m) = K(q_e, \gamma_m) - K(0, \gamma_m) = K(q_e, \gamma_m) - c(\gamma_m) \tag{13}$$

In order to calculate $K(q_e, \gamma_m)$, we use the inverse Laplace transform relation between probabilities and moments:

$$e^{K(q_e, \gamma_m)} = \int e^{-q_m \gamma_m \log \lambda_m} e^{K(q_e, q_m)}\, dq_m \tag{14}$$

Below, we show how such calculations can be performed analytically in the case of the log-normal multifractals (which are apparently a good approximation to the

Aggregation, Generalization, Upscaling:

(Measurement Scale Smaller than the estimated scale):

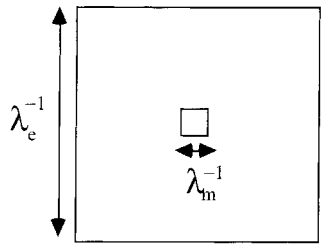

Conditional moments:

$$\left\langle \phi_{\lambda_e}^{q_e} \right\rangle_{\gamma_m} = \lambda_e^{K^*(q_e)} \lambda_e^{q_e\left(\gamma_m + C_1^*\right)}$$

Conditional probability distributions:

$$\Pr\left(\phi_{\lambda_e} > \lambda_e^{\gamma_e} \middle| \gamma_m\right) \approx \lambda_e^{-c^*\left(\gamma_e - \gamma_m - C_1^*\right)}$$

$$C_1^* = C_1\left(1 - \zeta^{-1}\right); \qquad \zeta = \log \lambda_m / \log \lambda_e > 1$$

(*c*)

$\alpha \approx 2$ empirical radiances discussed in the previous subsection); all we will require are the two-point cross-moments which are derived in appendix B. Using the lognormal $K(q_e, q_m)$ from appendix B, we finally obtain

$$K(q_e|\gamma_m) = C_1 \log \lambda_e (q_e^2(1-\varphi^2) - q_e) + q_e(C_1 + \gamma_m)\varphi \sqrt{(\log \lambda_e)(\log \lambda_m)} \qquad (15)$$

where φ is the correlation coefficient between the estimated and the measured singularities. For example, in the limit where there is a large difference in resolution, $\varphi \approx 0$, and we obtain the usual unconditional moments.

To understand the meaning of the above, consider now the special cases where the measured and estimated singularities are centred at the same location ($\Delta x = 0$; see appendix B, equation (B8)). In this case, we have the following simplification:

$$\varphi = \frac{\log(\min(\lambda_e, \lambda_m))}{\sqrt{\log \lambda_e \log \lambda_m}} \qquad (16)$$

which has the expected property that $\varphi = 1$ if $\lambda_e = \lambda_m$ and $\varphi \approx 0$ in the limit where the ratio between the resolutions is very large. We can thus consider the following cases.

(i) *Disaggregation/downscaling: the measurement scale is larger than the estimated scale* ($\lambda_e > \lambda_m$)

In this case, we measure the average over a large scale and wish to extrapolate

Objective analysis/Interpolation: Measurement Scale equal to the estimated scale:

$$\lambda=\lambda_m=\lambda_e$$

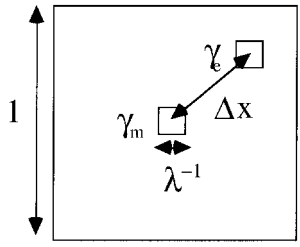

Conditional moments:

$$\left\langle \phi_\lambda^q \right\rangle_{\gamma_m} \approx \lambda^{K(q)} \Delta x^{K(q)-q\gamma_m} \qquad 1 \geq \Delta x \geq \lambda^{-1}$$

Conditional probability distribution:

$$\Pr\left(\phi_\lambda > \lambda^{\gamma_e} \middle| \gamma_m\right) \approx \lambda^{-c\left(\gamma_e|\gamma_m\right)}$$

$$c\left(\gamma_e|\gamma_m\right) = \frac{\left(\gamma_e - \varphi\gamma_m + C_1(1-\varphi)\right)^2}{4C_1\left(1-\varphi^2\right)} = \frac{c\left(\gamma_e - \varphi(\gamma_m + C_1)\right)}{\left(1-\varphi^2\right)} \qquad \varphi \approx -\frac{\log \Delta x}{\log \lambda}$$

(*d*)

to much smaller scales (recall that the scale ratio λ is inversely proportional to length; see figure 8(*b*)). Using equation (16), we obtain $\varphi^2 = \log \lambda_m / \log \lambda_e$ and

$$\left\langle \phi_{\lambda_e}^{q_e} \right\rangle_{\gamma_m} = \left(\frac{\lambda_e}{\lambda_m}\right)^{K(q_e)} \lambda_m^{q_e \gamma_m} \tag{17a}$$

The interpretation of this is simple: the q_eth power of the measured value $\lambda_m^{\gamma_m}$ is modulated by a prefactor which is the q_eth moment over the scale ratio λ_e/λ_m over which the extrapolation is made. This result can also be obtained directly from the factorisation property of conservative multifractals; the large-scale multiplicatively modulates the small; therefore it holds for all conservative multifractals.

This leads to the following conditional probabilities:

$$\Pr(\phi_{\lambda_e} > \lambda_e^{\gamma_e} | \gamma_m) \approx \lambda_e^{-(1-\zeta)c((\gamma_e - \zeta\gamma_m)/(1-\zeta))} \tag{17b}$$

where

$$\zeta = \frac{\log \lambda_m}{\log \lambda_e}$$

(ii) *The measurement scale is smaller than the estimated scale* ($\lambda_e < \lambda_m$)

This result corresponds to the more frequent situation where, for example, *in situ* measurements are made at small scales and we seek to generalise to larger scales; it

Conditional autocorrelations and spectra:

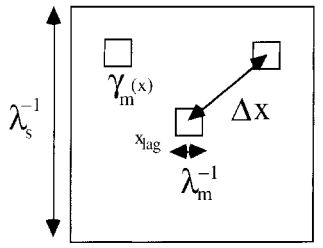

Spatially averaged over the lag position x_{lag}:

$$\left\langle \overline{\phi_{\lambda_m}(x_{lag})\phi_{\lambda_m}(x_{lag}+\Delta x)|\gamma_m(x)} \right\rangle \approx \Delta x^{-\gamma_m + C_1\zeta} \qquad \gamma_m > 3C_1$$

$$\zeta = \frac{\log \lambda_s}{\log \lambda_m} \qquad \zeta < 1$$

$$E(k) \approx k^{-\beta}$$

$$\beta_{cond} = 1 - \gamma_m + C_1\zeta$$

compare this to the usual unconditional result:

$$\beta_{uncond} = 1 - 2C_1$$

(*e*)

is less obvious to interpret (figure 8 (*c*)). Here, we have $\varphi^2 = \log \lambda_e / \log \lambda_m$; using this in equation (16), we obtain

$$\left\langle \phi_{\lambda_e}^{q_e} \right\rangle_{\gamma_m} = \lambda_e^{K^*(q_e)} \lambda_e^{q_e(\gamma_m + C_1^*)} \tag{18a}$$

with corresponding conditional probablility

$$\Pr(\phi_{\lambda_e} > \lambda_e^{\gamma_e} | \gamma_m) \approx \lambda_e^{-c^*(\gamma_e - \gamma_m - C_1^*)} \tag{18b}$$

where the asterix means the 'renormalised' functions with parameter

$$C_1^* = C_1(1 - \zeta^{-1}) \tag{18c}$$

In equation (18a), the second term simply represents the direct extrapolation of the measured singularity to the large scale ($\lambda_e^{\gamma_m}$). It is modulated by a prefactor that represents a systematic γ_m independent bias and which disappears for $\lambda_e \approx \lambda_m$. For example, assuming that the scaling extends to planetary scales ($L \approx 10^7$ m) and that $C_1 \approx 0.05$ (see table 1), we find that *in situ* pigment concentration measurements at 1 m resolution ($\lambda_m \approx 10^7/1 = 10^7$) extrapolated to 1 km ($\lambda_e \approx 10^7/10^3 = 10^4$; the CZCS scale; see below) yield a bias in the mean ($q_m = 1$) of factor ≈ 8 in the value $\lambda_e^{\gamma_m}$, which itself represents a systematic bias by the γ_m dependent factor $(\lambda_e/\lambda_m)^{\gamma_m}$.

3.2. *Multifractal objective analysis*

The correlations/interrelations[22] between singularities can be used for useful purposes other than downscaling or upscaling. Consider a variant on the resolution problem above in which the points are seperated by a distance Δx non-dimensionalised by dividing by the outer scale L so that Δx varies between the pixel scale ratio Λ^{-1} and 1; we seek to infer the value of the field at a neighbouring pixel using a measured value of the field a distance Δx away. For simplicity, take the resolutions as identical; $\lambda_e = \lambda_m = \lambda$; this is a special case of the problem of objective analysis in which the values of many measurements are used to estimate the conditional expectations at data sparse regions. If our object is only to correct the statistical properties for biases due to measurement sparseness, then such statistical multifractal objective analysis is relatively straightforward (Tessier *et al.* 1994). However the conditional expectation discussed here corresponds to the more usual problem of objective analysis on individual realisations, which is much more difficult (see, however, Salvadori (1993) and Salvadori *et al.* (1993, 2000)). Here, we show how a simple extension of the above can be used to obtain optimum information from single measurements in conservative lognormal multifractals[23].

First, consider the specialisation of equation (16) to the case where $\lambda_e = \lambda_m = \lambda$; we obtain the conditional expectation

$$\left\langle \phi_\lambda^{q_e} \right\rangle|_{\gamma_m} = \lambda^{K(q_e) - K(q_e \varphi) + q_e \varphi \gamma_m} \tag{19}$$

where $\varphi(\Delta x)$ is the correlation of known and inferred/estimated singularities (see appendix B). Note that, as expected, when $\varphi = 0$ (long distance), we obtain the usual unconditional result; whereas, when $\varphi = 1$ (the short distance limit), we obtain the measured result $\lambda^{q\gamma_m}$.

In the scaling regime, we have the following approximation which can be obtained by expanding the cosine equation (B8) about $|k| \approx 0$:

$$\varphi(\Delta x) \approx \frac{-\log \Delta x}{\log \lambda} \tag{20}$$

Now define the 'extrapolation/forecasting[24] scale' $\lambda_f = \lambda \Delta x$ as the ratio of the actual forecast distance Δx to the resolution λ^{-1}. Using equation (20), we obtain

$$\left\langle \phi_\lambda^{q_e} \right\rangle|_{\gamma_m} \approx \lambda_f^{K(q_e) + c_1 \varphi} \left(\frac{\lambda}{\lambda_f} \right)^{q_e \gamma_m} \tag{21}$$

When $\Delta x = \lambda^{-1}$ (hence $\lambda_f = 1$), we have $\varphi(\Delta x) = 1$ (since the field is homogeneous over this distance); this shows how the expectation decays from the known value $\lambda^{q\gamma_m}$ to the unconditional expectation value $\lambda^{K(q)}$ (obtained with $\Delta x = 1$, i.e. $\lambda_f = \lambda$; see figure 8(d)).

We can also calculate the conditional co-dimension function $c(\gamma_e | \gamma_m)$ which

[22] For $\alpha < 2$, the usual correlation coefficient between singularites diverges since the γ values are infinite variance stable Levy random variables; however, they are still interrelated, equation (A4) still holds.

[23] Equation (A4) combined with equations (13) and (14) can be used in the general case; however except for log-normal multifractals analytic results are not generally possible.

[24] The term 'forecasting' would only be fully justified if one of the axes were the time axis. See Marsan *et al.* (1996) for detailed treatment of this problem.

determines the conditional probability distribution. The exact result can be obtained by Legendre transform of $K(q_m|\gamma_m)$:

$$c(\gamma_e|\gamma_m)=\frac{(\gamma_e-\varphi\gamma_m+C_1(1-\varphi))^2}{4C_1(1-\varphi^2)}=\frac{c(\gamma_e-\varphi(\gamma_m+C_1))}{(1-\varphi^2)} \tag{22}$$

When $\varphi\approx\log\Delta x/\log\lambda\ll 1$ (long range extrapolation/forecast; $\lambda_f\gg 1$), we obtain the following approximation (valid to first order in φ) for the conditional co-dimension function:

$$c(\gamma_e|\gamma_m)=c(\gamma_e-\varphi(\gamma_m+C_1)) \tag{23}$$

which shows how the unconditional co-dimension ($c(\gamma_e)$) is modified by the measurement; the distribution of singularities is slightly shifted as a function of φ and the measured singularity fluctuation[25] (γ_m+C_1). The case of short range extrapolation ($\varphi\approx 1$) requires a bit more care. Defining the small quantity $\Delta=1-\varphi$, we obtain

$$c(\gamma_m|\gamma_m)\approx\frac{(\gamma_e-\gamma_m)^2}{8C_1\Delta} \tag{24}$$

which shows that $\gamma\approx\gamma_m$ as expected for sufficiently short range extrapolations/forecasts.

In practice, although it is important to obtain an estimate of the optimum extrapolation/forecast value, one also seeks to characterise the expected root-mean-square (RMS) error in the estimate. This is also straightforward to obtain using the above formulae. For example, we can now define the relative RMS error for the extrapolation of the qth moment:

$$E_q^2=\frac{\langle\phi_\lambda^{2q}\rangle|_{\gamma_m}}{\langle\phi_\lambda^q\rangle^2|_{\gamma_m}}-1=\lambda^{K(2q)-2K(q)-(K(2q\varphi)-2K(q\varphi))}-1=\lambda^{2C_1q^2(1-\varphi)}-1 \tag{25}$$

Using equation (20) for φ, we obtain

$$E_q^2+1=\lambda_f^{2C_1q^2} \tag{26a}$$

For example, for the fluorescence plankton surrogate, we have $C_1\approx 0.05$ (table 2); hence, for the mean ($q=1$), we obtain

$$E_1=\sqrt{\lambda_f^{2C_1}-1} \tag{26b}$$

so that *in situ* concentration values at 1 m resolutions extrapolated to a location 1 km away (e.g. the opposite side of a CZCS pixel) requires $\lambda_f=1\,\text{km}/1\,\text{m}=10^3$ and yields an RMS error in the mean of $\approx 170\%$. However, the relative RMS eror in extrapolating the variance will be much larger; taking ($q=2$) we obtain

$$E_1=\sqrt{\lambda_f^{4C_1}-1} \tag{26c}$$

i.e. $\approx 400\%$.

[25]For the log-normal multifractal, γ is a Gaussian random variable with $\langle\gamma\rangle=-C_1$, $\langle\gamma^2\rangle=2C_1$; hence, $\gamma+C_1$ is the fluctuation in the singularity value about the mean.

3.3. *Conditional autocorrelations and spectra: biased exponents and spurious breaks in the scaling*

We are often interested in remotely studying phenomena which are both extreme and rare, e.g. using infrared imagery to study volcanic 'hot spots' (Gaonac'h *et al.* 1999, Harvey *et al.* 1999). In this case, we may have one or a few pixels which are far more intense than their neighbours and appear as nearly a 'δ function' (e.g. a lava lake). The resulting autocorrelations and spectra will generally be biased; for example, in the extreme case of a true δ function, the spectrum would be flat[26]. In order to quantify the resulting statistical biases, we must therefore consider conditional autocorrelations and conditional spectra (obtained from the latter by Fourier transform). Finally, when studying such extremes, we often are not so interested in studying ensemble statistics (the statistics of the extremes may not be too reliable anyway), but rather single realisation statistics, e.g. the spectrum of a single satellite picture of an active volcano. In this case, we will need to consider the variability about the ensemble mean.

In appendix C, by using three-point statistics we show how to estimate the corresponding conditional statistics for the case of log-normal multifractals (see figure 8(*e*)). The main result is that, if we condition the statistics to the presence of a sufficiently large order of singularity ($\gamma_m > 3C_1$), we obtain (see equation (C11))

$$\overline{\langle \phi_{\lambda_m}(\mathbf{x}_{\text{lag}})\phi_{\lambda_m}(\mathbf{x}_{\text{lag}}+\Delta\mathbf{x})\gamma_m(\mathbf{x})\rangle} \approx \Delta x^{C_1\zeta-\gamma_m} \tag{27}$$

where the overbar indicates spatial averaging over all $\mathbf{x}_{\text{lag}}$ locations in the satellite picture (overall size, λ_s^{-1} with pixel size λ_m^{-1}) and here and in the rest of this subsection, $\zeta = (\log \lambda_s)/(\log \lambda_m)$. Since the unconditional exponent of Δx is $-2C_1$, this shows that there is a shift in the exponent so that the effect of the conditioning is to roughen the spectrum by the same amount as a fractional integration of order ΔH:

$$\Delta H = C_1\left(1+\frac{\zeta}{2}\right)-\frac{\gamma_m}{2} \tag{28}$$

Since this result is valid only for $\gamma_m > 3C_1$, since $\lambda_s < \lambda_m$, we find $\zeta < 1$; hence $\Delta H < 0$ (corresponding to a fractional differentiation), indicating that the effect of this conditioning is indeed to flatten the spectrum.

When the conditioning order of singularity is not so great (in the range $(4\zeta - 1) < \gamma_m < 3C_1$), only the short distances will have anomalous scaling; therefore, we obtain a spurious scaling break. However, as indicated in appendix C, on spectra from individual realisations of the multifractal process, these relatively low γ_m effects may be quite hard to make out above the noise, so this result may not be too significant in practice.

To make this discussion concrete, let us further consider volcanoes and extreme hot spots, e.g. regions with temperatures $> 800C$. For illustrative purposes, assume that the outer scale is 10^4 km, resolution 10 m ($\lambda = 10^4$ km/10 m $= 10^6$) and at any given moment, there are 10 pixels of this size somewhere on the planet showing such a temperature (corresponding for example to lava lakes). Assuming the Earth's

[26]The exact slope would depend somewhat on the assumed statistics of the δ function, Gaussian or Levy.

surface area is $\approx 10^{14}\,\mathrm{m}^2$, then the probability of a given $10\,\mathrm{m}\times 10\,\mathrm{m}$ pixel exceeding this temperature would be

$$p(\gamma_m)=\lambda^{-c(\gamma_m)}\approx 10/(10^6)^2=10^{-11} \tag{29a}$$

hence

$$c(\gamma_m)\approx 11/6=1.83 \tag{29b}$$

We can attempt to estimate the maximum order of singularity from this probability by using the C_1, α values estimated by Gaonac'h *et al.* (1999) and Harvey *et al.* (1999); very roughly, they obtained $C_1=0.1$, $\alpha=2$. Using these values and equation (29b) in equation (4b), we obtain $\gamma_m\approx 0.75$. If we now consider an infrared picture with 1000 pixels on a side (each 10 m), then $\lambda_s=10^3$. Using equation (28), the bias $2\Delta H$ in the spectral exponent is thus ≈ 0.5.

3.4. *Vector multifractals: calibration of remotely sensed data and the resolution dependence of principle component analysis*

We are frequently faced with two (or more) interrelated datasets. For example, principle component analysis uses several wavelength channels of the same scene to determine covariance matrices and hence eigenvectors (principle components) which define uncorrelated[27] linear combinations of the different channels. A related example which we develop in detail, is the problem of comparing *in situ* measurements with surrogates derived from remotely sensed radiances, with the former being used for calibrating the algorithm. In subsection 3.1, we have seen how for a known (e.g. satellite field) one can extrapolate from one resolution to another (e.g. to the calibration scale). However, at best, we expect the measurements and surrogates (denoted P,S for 'plankton' and 'surrogate') to have non-linear but scaling statistical relations due to complex non-linear (coupled cascade) processes from large to small scales. This statistical relationship between P,S is very poorly discerned by traditional cross-correlation analysis which is performed at a single resolution; in fact, below, in accord with the empirical findings of Chou (1991) on the autocorrelations mentioned above, we show that even the sign of the cross-correlations can change as a function of resolution. Similarly, we shall see that, in general, the principle components will be scaling functions of the resolution. Since satellite resolution is fairly arbitrary, this considerably diminishes their significance at any fixed resolution; on the contrary, augmenting the importance of the corresponding (resolution invariant) exponent.

The simplest way to to treat scaling interrelations is to introduce the state vector $\mathbf{v}_\lambda=(P_\lambda, S_\lambda)$ at resolution[28] λ; we then can relate the large-scale and small-scale vectors by a matrix (rather than by the usual scalar):

$$\mathbf{v}_\lambda=\lambda^{\gamma}\mathbf{v}_1 \tag{30}$$

where here γ is a random, 2×2 matrix singularity (2×2 matrices are indicated in bold). Note that here we assume that $\mathbf{v}_\lambda$ is the direct result of a multiplicative cascade (i.e. $H=0$). Just as in the scalar case, it is more realistic and general to consider the observed components to be fractional integrals with respect to such a process; for

[27] As we see in the example below, although their covariance may be zero, they can nevertheless have a strong statistical dependence.

[28] These must first be suitably non-dimensionalized, e.g. using the mean.

simplicity, we do not treat this complication here. The framework for handling such vector and matrix processes is Lie cascades (Schertzer and Lovejoy 1995).

To see how this works; make the following pseudoquaternion decomposition:

$$\mathbf{1}=\begin{pmatrix}1 & 0\\ 0 & 1\end{pmatrix} \quad \mathbf{I}=\begin{pmatrix}0 & -1\\ 1 & 0\end{pmatrix}$$

$$\mathbf{K}=\begin{pmatrix}1 & 0\\ 0 & -1\end{pmatrix} \quad \mathbf{J}=\begin{pmatrix}0 & 1\\ 1 & 0\end{pmatrix}$$

$$\gamma=\mathbf{1}_{\gamma_1}+\mathbf{I}_{\gamma_I}+\mathbf{J}_{\gamma_J}+\mathbf{K}_{\gamma_K} \tag{31}$$

so that the γ_1, γ_K, γ_J, γ_I are the (random) coefficients of the various basis matrices. Note that $\mathbf{I}^2=-\mathbf{1}$, $\mathbf{J}^2=\mathbf{K}^2=\mathbf{1}$. Just as in the scalar case, the statistical properties of the process can then be specified via the second (Laplace) characteristic function (now of a scalar function of a matrix moment $\mathbf{Q}$):

$$\lambda^{K(Q)}=\left\langle \lambda^{Tr(\mathbf{Q}\cdot\gamma)}\right\rangle \tag{32}$$

where $Tr(\mathbf{Q}\cdot\gamma)$ indicates the trace of the matrix product $\mathbf{Q}\cdot\gamma$. In order to understand the complexity of the resulting behaviour, recall the following formula (e.g. Schertzer and Lovejoy 1985) for the exponentiation of a 2×2 matrix:

$$\lambda^{\gamma}=\lambda^{\gamma_1}\left(\mathbf{1}\cosh au+\frac{(\gamma-\gamma_1 1)}{a}\sinh au\right) \tag{33}$$

with

$$a^2=\gamma_K^2+\gamma_J^2-\gamma_I^2$$

$$u=\log\lambda \tag{34}$$

Note that, when $a^2<0$, the cosh and sinh are replaced by cos, sin and a by $|a|$ in the above.

We now calculate the cross-correlation coefficient of P_λ, S_λ as functions of λ, showing how it can periodically change sign at fixed factors of resolution. For simplicity, consider a process involving only the commuting components γ_1, γ_I. In this case, equation (33) reduces to

$$\lambda^{\gamma}=\lambda^{\gamma_1}(\mathbf{1}\cos u\gamma_1+\mathbf{I}\sin u\gamma_1) \tag{35}$$

We can see that the use of the symbol $\mathbf{I}$ is not accidental; the sub-algebra it generates corresponds to the algebra of complex numbers, the 'complex cascades' discussed in Schertzer and Lovejoy (1995). Therefore, it is advantageous to use the complex notation $z_\lambda=P_\lambda+iS_\lambda$; $\gamma=\gamma_1+i\gamma_I$, with $i^2=-1$; thus

$$z_\lambda=\lambda^{\gamma}z_1 \tag{36}$$

These rather special complex processes, therefore, describe a vector whose length is determined by the random modulus λ^{γ_1} and random angle $\gamma_I \log\lambda$; the measured surrogate (S_λ) and inferred/estimated quantity (P_λ) are simply different components of the resulting random vector. In this example, the problem of estimation from the known surrogate is equivalent, therefore, to that of using the statistics of the vector length and angle as a function of scale to obtain the conditional expectation of one of the vector components given another orthogonal component.

The statistics can now be defined by the following:

$$\langle \lambda^{q\gamma_1} \rangle = \lambda^{K_1(q)}$$
$$\langle \lambda^{iq\gamma_I} \rangle = \lambda^{K_I(q)} = \lambda^{K_{I,R}(q) + iK_{I,J}(q)} \tag{37}$$

Note that the Laplace second characteristic function $K_1(q)$ is purely real, while the Fourier transform yields a generally complex second characteristic function $K_I(q)$ as indicated. Note further that the conservation condition $\langle \lambda^{\gamma} \rangle = 1$ implies $K_1(1) + K_I(1) = 0$ and $\langle P_\lambda \rangle = P_1$, $\langle S_\lambda \rangle = S_1$. Schertzer and Lovejoy (1995) showed how complex cascades can be generated with extremal Levy λ_1, but with non-extremal Levy λ_I (this is indeed necessary to obtain non-zero $K_{I,I}(q)$).

We shall now calculate the cross-correlation coefficient between the vector components. For example, to calculate the cross-variance, we can take the ensemble average of the relation $2P_\lambda S_\lambda = \mathrm{Im}(z_1^2)$. Doing this and using the above definitions of the characteristic functions, we obtain

$$\langle P_\lambda S_\lambda \rangle - \langle P_\lambda \rangle \langle S_\lambda \rangle = \frac{R_1^2}{2} [\lambda^{K_1(2) + K_{I,R}(2)} \sin(K_{I,I}(2) \log \lambda + 2\theta_1) - \sin(2\theta_1)] \tag{38a}$$

where $R_1 e^{i\theta_1} = z_1 = P_1 + iS_1$ is the initial large-scale ($\lambda = 1$) vector. The combination of the convexity of second characteristic functions and the conservation condition shows that $K_1(2) + K_{I,R}(2) > 0$; hence, as λ increases, the constant term $\sin 2\theta_1$ becomes negligible and the sign of the above (centred) cross-correlation oscillates with period $\log \lambda$. To complete the calculation, we work out the cross-correlation coefficient:

$$\rho_{PS,\lambda} = \frac{\langle P_\lambda S_\lambda \rangle - \langle P_\lambda \rangle \langle S_\lambda \rangle}{\sigma_{P,\lambda}\, \sigma_{S,\lambda}} \tag{38b}$$

where the σ are the standard deviations given below:

$$\sigma_{P,\lambda}^2 = R_1^2 \left[\lambda^{K_1(2) + K_{I,R}(2)} \cos^2\left(\frac{K_{I,I}(2)}{2} \log \lambda + \theta_1 \right) - \cos^2(\theta_1) \right]$$
$$\sigma_{S,\lambda}^2 = R_1^2 \left[\lambda^{K_1(2) + K_{I,R}(2)} \sin^2\left(\frac{K_{I,I}(2)}{2} \log \lambda + \theta_1 \right) - \sin^2(\theta_1) \right] \tag{39}$$

As $\lambda \to \infty$, the product $\sigma_{P,\lambda}\sigma_{S,\lambda}$ approaches $R_1^2/2\, \lambda^{K_1(2) + K_{I,R}(2)} |\sin(K_{I,I}(2) \log \lambda + 2\theta_1)|$; hence, $\rho_{PS,\lambda} \approx \pm 1$ alternating in sign every factor of $e^{\pi/K_{I,I}(2)}$. The interpretation of this is that, when λ is large, the components of the vector are typically of comparable magnitude, with signs depending on the quadrant in which they fall; $K_{I,I}$ quantifies the rotation of the centre of the distribution of angles with scale (and hence the quadrant).

We may now use this example to consider the resolution effect on the principle components in a dual-channel analysis where P, S represent two radiances. Denoted by θ_c, the angle of one of the eigenvectors/ principle-components with respect to the P axis of the covariance matrix of P, S, we obtain

$$\sin^2(2\theta_c) = \frac{(\rho_{PS,\lambda}\, \sigma_{P,\lambda}\, \sigma_{S,\lambda})^2}{\left(\frac{\sigma_{P,\lambda} - \sigma_{S,\lambda}}{2} \right)^2 + (\rho_{PS,\lambda}\, \sigma_{P,\lambda}\, \sigma_{S,\lambda})^2} \tag{40a}$$

Using equations (38) and (40), when λ is large, we obtain

$$\theta_c \approx \theta_1 + \frac{K_{1,1}(2) \log \lambda}{2} \tag{40b}$$

showing that the principle components continuously rotate with a constant (logarithmic) rate with resolution.

This example clearly shows the danger of making quantitative or even qualitative inferences about the relation of two processes from the correlations/covariances at fixed resolutions.

4. Ocean colour and phytoplankton biomass by remote sensing

4.1. *The standard resolution-dependent approach*

The use of ocean colour to infer ocean properties is a branch of marine optics that received major impetus in the 1960s and 1970s due to the advent of satellite remote sensing, the highlight of which was the roughly 1 km resolution, four-channel CZCS sensor which was operational from 1978 to 1986 (see the papers in Barale and Schlittenhardt (1993)). One of the significant uses of the CZCS sensor was to estimate the density of chlorophyll-like pigment (which is a phytoplankton surrogate). Of the four relatively narrow channels, one is particularly sensitive to cholorophyll and another is particularly insensitive (a reference band); these correspond very closely to MIES channels 7 and 8, respectively. The basic idea (explained in detail in Sturm (1993)) is to use information from the other two CZCS channels to provide corrections (to account for both additive aerosol and surface scattering effects as well as for multiplicative atmospheric transmission effects). This information is used in a semi-empirical formula for estimating the chlorophyll-like pigment concentration from the (corrected) pigment sensitive reflection (R_p) and the reference reflection (R_r). To express the semi-empirical[29] formula, it is then usual to introduce the reflectance ratio X:

$$X = R_p / R_r \tag{41}$$

which has the property of being insensitive to sun and satellite angles, as well as to overall atmospheric absorption. If the additive and multiplicative corrections are nearly uniform across the scene, then the multifractal parameters estimated in the previous sections will correspond to those of the reflection coefficients, since the spectral and DTM techniques are not affected by a linear transformation. In the following, to simplify the discussion, we therefore assume that R_p and R_r have the same scaling properties as the measured MIES channel 7 and 8 radiances.

The 'standard' CZCS algorithm is based on single scattering theory and other approximations that are used to obtain relations for the pigment concentration surrogate S, of the form

$$\log S = \sum_{i=0}^{3} a_i (\log X)^i \tag{42}$$

with the a_i determined empiricially from estimates of *in situ* pigment concentrations P by regression of P versus the remote surrogate S. For example, Sturm (1993) with CZCS sensor in 'type 1 waters' obtains $a_0 = 0.768$, $a_1 = 2.61$, $a_2 = 0.791$, $a_3 = -0.388$

[29] We use the term 'semi-empirical' to denote algorithms which may have some physical motivation but which involve various *ad hoc* assumptions or approximations.

(logs to base 10). Since we have found that R_p and R_r are multifractal, they are each strongly resolution dependent; hence, *a priori*, so will be their ratio X. Therefore, we anticipate that the empirical a_i values will have different scalings from each other (different functions of λ) since $\log X$, $(\log X)^2$ and $(\log X)^3$ will each have different scalings. We expect then, that observers using either *in situ* or remote data with other resolutions will obtain a different (subjective) set of a_i values.

4.2. *Scale-invariant calibration*

We have seen that P (as inferred from the *in situ* fluorescence measurements) and R_c and R_r (as inferred by the scaling of the radiances) are all strongly dependent on the resolution λ; hence, we expect that, in general, for the surrogate S to provide a good approximation to P at all scales (not just at the calibration scale), the a_i values should be functions of scale; *a priori*, this implies that one requires a series of empirical *functions* $a_i(\lambda)$, which, in the absence of any other information, corresponds to the impossible determination of an infinite number of empirical parameters.

The fundamental reason for introducing multifractals in remote sensing is precisely to circumvent these resolution-dependent quantities by introducing resolution-*independent* exponents (e.g γ, $c(\gamma)$, $K(q)$, etc.). In other words, we exploit the scale invariance to relate scale-invariant quantities derived from P to scale-invariant surrogate quantities derived from R_c and R_r using a scale-invariant function. The scale-invariant values of the field are the singularities

$$\gamma_P = \frac{\log P/\langle P \rangle}{\log \lambda}$$
$$\gamma_R = \frac{\log R/\langle R \rangle}{\log \lambda} \tag{43}$$

where we have used the ensemble means for normalisation. We can then obtain

$$\gamma_S = f(\gamma_{R_c}, \gamma_{R_r}) \tag{44}$$

where f is now an objective (observer independent) function. The resolution-independent estimator γ_S determined at the satellite resolution can then be compared to the resolution-independent *in situ* calibration values γ_P. Note that, since scale invariance is a statistical symmetry principle, we do not generally expect $\gamma_P = \gamma_S$ in the usual deterministic sense; rather, we expect $\gamma_P \overset{d}{=} \gamma_S$, where the symbol '$\overset{d}{=}$' indicates equality in probability distributions[30]. If f is parametrised, then resolution-independent regressions can be used to determine resolution-independent coefficients. As a simple example, consider the CZCS calibration problem, noting that, from equations (41–43),

$$\log X = \log \frac{\langle R_p \rangle}{\langle R_r \rangle} + (\gamma_r - \gamma_p) \log \lambda \tag{45}$$

Therefore, the semi-empirical formula for S can be rewritten in terms of the scale-invariant calibration parameters A_i:

$$\gamma_{P_e} = \sum_{i=0}^{3} A_i (\gamma_r - \gamma_p)^i \tag{46}$$

[30] $a \overset{d}{=} b$ means that $\Pr(a > s) = \Pr(b > s)$ for all thresholds s; 'Pr' indicates 'probability'.

where $A_i = a_i' \log \lambda$ and the a_i' are themselves polynomial functions of a_i. This shows that we expect the coefficients a_i to have complex polynomial dependence on the log resolution. Finally, if λ is known[31], this allows us to estimate the scale-invariant A_i values from the CZCS a_i values, obtaining a scale-invariant algorithm by using equation (43) to determine the surrogate S and then by using

$$\gamma_P \approx \gamma_S \tag{47}$$

as discussed below.

We now discuss the type of equality in equation (44), since it immediately introduces a statistical constraint which is important even when the measured and surrogate data are not simultaneous (as in this paper). Indeed, equations (43) and (44) imply, at the very least, that the '$\approx$' in equation (44) is taken as '$\stackrel{d}{=}$', i.e. that the probability distributions of γ_S and γ_P are identical. The relation $\gamma_S \stackrel{d}{=} \gamma_P$ is a fairly minimal requirement; in practical remote sensing algorithms, the much stronger deterministic equality $P = S$ is used (this is a special case of $\gamma_S \stackrel{d}{=} \gamma_P$). In either case, if the $c(\gamma)$ or $K(q)$ functions are known (in the case of universal multifractals, the latter are determined from H, C_1 and α), we require that the corresponding H, C_1 and α for P and S be equal. This requirement that the statistics of P and S be the same at all scales can be taken into account in the initial stages of semi-empirical algorithm development.

For example, the analyses presented earlier showed that α, C_1 and H are roughly same for *in situ* fluorescence and remotely sensed images. This suggests that derived pigment concentration should be obtained from a transformation that also preserves the universal multifractal parameters. For simplicity, consider once again conservative multifractals, $H = 0$ (if H is non-zero, the following will apply to the absolute gradients for which $H = 0$).

Consider an algorithm that consists of taking weighted powers of the reflectivities R at various channels (indexed by i):

$$S_\lambda = \prod_i b_i R_{i,\lambda}^{\alpha_i} \tag{48}$$

This algorithm is equivalent to a linear transformation of the singularities; if we assume that the different channels are statistically independent with identical α values, we can exploit the basic stability property of stable Levy variables. This stability property implies that the weighted sum of independent Levy variables with the same α values is another stable Levy with the same α but with C_1 transformed as

$$C_{1,S} = \sum_i C_{1i} a_i^\alpha \tag{49}$$

thus providing a constraint on the possible values of the[32] a_i.

---

[31] Note that the relevant resolution of data is its space/time resolution. Hence, *in situ* measurements at 'points' in space (which are invariably averaged over finite times) are not point measurements in space/time and have finite, not infinite, λ.

[32] Note that, in equation (49), the a_i values were assumed positive. If $\alpha = 2$, then we may use the modulus of a_i; otherwise, for $\alpha < 2$ the negative statistical moments of S will diverge so that we require $a_i > 0$.

4.3. *Implications for scale-invariant phytoplankton algorithms*

If a remote sensing algorithm is to provide a reliable surrogate of plankton concentration, we have seen that a necessary (but not sufficient!) condition is that the surrogate must have the same statistical properties as the plankton at all scales[33]. We have seen that this scaling condition can be profitably used to limit the types of possible algorithms.

Let us first consider the case where there is no break in the scaling. In this case, if the remote and *in situ* parameters were identical, (and this is consistent with the analyses above), the scale-by-scale statistical properties of the radiances and the fluorescence would be the same. However, standard remote plankton estimating algorithms use non-linear relations at the finest scale which will break the scaling and alter the statistics. It is easy, however, to devise other relations (such as those involving products of powers of field gradients) that would be scale invariant.

Because of the break, the actual situation is less favourable, since extrapolating to the smallest scale of variability requires knowledge of the break scale. Recall that Claeredeboudt *et al.* (2000) and Lovejoy *et al.* (2000) found that there was a break at the 'planktonoscale' that was highly variable[34] but was often in the vicinity of 100 m. Furthermore, rather than becoming homogeneous at the planktonoscale, the scaling was simply changed, with the concentration field becoming *more* rather than less variable at higher spatial frequencies, with this high level of variability continuing down to the smallest observed scales (≈ 1 m) but presumably being cut-off at centimetre scales by viscosity! The simplest model for this would be to assume that the the high-frequency and low-fequency multifractal parameters are fixed, as well as the true inner homogeneity scale. In this case, knowledge of the planktonoscale becomes fundamental in extrapolating to finer resolutions and hence for both calibration and plankton estimates. This indicates that (contrary to the CZCS) the sensor resolution must be of the order of 100 m or better (more study of the variability of this scale is required; it may frequently be much smaller). It would be interesting to test these ideas using simultaneous ocean colour and *in situ* measurements.

5. Conclusions

We have argued that geophysical and geographical fields are extremely variable over ranges of up to 10 orders of magnitude in scale, but that they nevertheless respect a (non-classical) scale-invariant symmetry principle leading to multifractal fields and strong power law resolution dependencies. Over the last 12 years, empirical analyses of atmospheric, land and ocean surface fields at visible, infrared and microwave wavelengths, have confirmed these ideas for various scale ranges, some as small as 1 m (lidar rain, Lovejoy and Schertzer 1991), cloud radiances (Lovejoy *et al.* 1997, Sachs *et al.* 2000 , Stanway 2000)) and some as large as 5000 km (infrared and visible radiances (Lovejoy *et al.* 1997)). This theoretically predicted and empirically observed, wide range scaling renders traditional remote sensing algorithms strongly scale/resolution dependent. Mathematically, it corresponds to the fact that the corrsponding mathematical measures are singular with respect to the usual Lebesgue measures. At first glance, it is perceived as a subjective observer dependence that is

[33] Even if this criterion is satisfied, the two series may nevertheless be statistically independent of each other, in which case S would have no information about P.

[34] They argued that this scale was determined by predator/prey type interactions and was thus influenced by the highly variable (intermittent) velocity field.

an increasingly significant barrier to quantitative exploitation of remotely sensed data. We argue that wide range scaling *demands* the development of new objective (observer/resolution-independent) algorithms and techniques. These techniques are based on the existence of two scale-invariant generators. The first (discussed here) is a statistical generator that determines the statistical properties of the field (including all joint n point probabilities) as functions of scale. The second (discussed elsewhere) determines the notion of scale itself and is necessary because geophysical scaling is not isotropic; the corresponding fractals and multifractals are not self-similar; here, we used isotropic analysis techniques, implicitly making the approximation that they were self-similar.

In order to indicate how scale-invariant algorithms can be developed, and to show the limits of current non-scaling approaches, we studied the example of ocean colour using an eight-channel, 7 m resolution dataset from the St Lawrence estuary (sensitive to chlorophyll-like pigment). We first showed that the various channels indeed had wide range scaling which we quantified over roughly four orders of magnitude in scale, obtaining multifractal parameters very similar to those observed by *in situ* measurements. In section 3, we provided some simple examples demonstrating how multifractals can used to answer basic resolution problems in remote sensing; in particular, we showed how to extrapolate from one resolution to another and from one location to another. We quantitatively, showed how the study of special extreme and rare events can lead to biased exponents and spurious breaks in the scaling. We also showed some of the pitfalls of conventional (fixed resolution) statistics, going into detail through a simple example where not only the magnitude but also the sign of the cross-correlation between the surrogate and the measurement can change with resolution, and in which even the angles of the principle components change linearly with the log of resolution. In section 4, we showed that the standard CZCS pigment concentration algorithm had hidden resolution dependencies and indicated how these could be removed to obtain a resolution-independent algorithm.

Appendix A: Cross-moments, correlations and spectra of multifractals

A frequently used characterisation of scale-by-scale variability is the energy/power spectrum which (for statistically translationally invariant processes, via the Wiener Khintchine theorem), is the Fourier transform of the autocorrelation function. Since the autocorrelation function is a second-order statistic, and statistics of all orders are generally important in multifractals, the autocorrelation is not as fundamental a quantity as it is in (non-intermittent) quasi-Gaussian statistics where the autocorrelation function/spectrum determines essentially all the variability.

We start with an argument (Monin and Yaglom 1975) for discrete cascade processes on the unit interval (the dimension of space is unimportant; we can take it to equal 1 here). Consider a discrete cascade with ratio λ_0; n cascade steps (external scale ratio $\lambda = \lambda_0^n$). Define the cross-correlation function $\rho_n(q_1, q_2, \Delta x)$ and cross-correlation exponent $K(q_1, q_2)$:

$$\rho_n(q_1, q_2, \Delta x) \equiv \lambda^{K(q_1, q_2)} = \langle \phi_n^{q_1}(x) \phi_n^{q_2}(x + \Delta x) \rangle \tag{A1}$$

(this is only a function of the seperation Δx, since the cascade is approximately statistically translationally invariant. Continuous cascades are exactly translational invariant).

If we take $\Delta x = \lambda_0^{-m}$, then the points x, $x+\Delta x$ (typically) share m parent eddies; they have m multiplicative factors ($\mu\phi$) the same, n–m different; therefore, we obtain

$$\rho_n(q_1, q_2, \Delta x) = \langle \mu\phi^{q_1+q_2} \rangle^m \langle \mu\phi^{q_1} \rangle^{n-m} \langle \mu\phi^{q_2} \rangle^{n-m} \tag{A2}$$

Hence, using the fact that $\langle \mu\phi^q \rangle = \lambda_0^{K(q)}$ (and, for $\lambda = \lambda_0^n$, switching to the notation $\rho_\lambda = \rho_n$):

$$\rho_\lambda(q_1, q_2, \Delta x) = \Delta x^{K(q_1)+K(q_2)-K(q_1+q_2)} \lambda^{K(q_1)+K(q_2)} \tag{A3}$$

Now, writing $\varphi = -\log \Delta x / \log \lambda$, we obtain

$$K(q_1, q_2) = (1-\varphi)(K(q_1)+K(q_2)) + \varphi K(q_1+q_2) \tag{A4}$$

Hence, we see that φ plays the role of a correlation coefficient; $\varphi = 0$ corresponds to complete independence, $\varphi = 1$ to complete dependence (however, only for log-normal multifractals is φ a true correlation coefficient). Obviously, this result can be generalised for the n point statistics, although it gets rapidly more complicated; see Schertzer *et al.* 1997 appendix C for some results on four-point statistics. For example, using the same method, we obtain the following formula for the three-point statistics:

$$\begin{aligned} K(q_1, q_2, q_3) = K(q_1, q_3) + (K(q_1, q_3) + K(q_2, q_3) - (1-\varphi_{123})(K(q_1)+K(q_2) \\ + K(q_3)) + \varphi_{123}(K(q_1+q_2+q_3) - K(q_1+q_2) \\ - K(q_1+q_3) - K(q_2+q_3)) \end{aligned} \tag{A5}$$

where $\varphi_{123} = \min(\varphi_{12}, \varphi_{13}, \varphi_{23})$ corresponds to the shared interrelation of the three points (φ_{ij} is the φ for the i, j pair of points).

In the special case of two-point lognormal statistics, $K(q) = C_1(q^2 - q)$, and we obtain

$$K(q_1, q_2) = C_1(q_1^2 - q_1) + C_1(q^2 - q^2) + 2C_1 q_1 q_2 \varphi \tag{A6}$$

In the lognormal case, considered in more detail in appendix B, we show that φ is indeed the correlation function for the singularities, and we generalise the above equation for the case where the resolutions are no longer equal to λ. See Schertzer *et al.* 1997 for a generalization to anisotropic space-time multifractals (especially appendix C).

A.2. *The spectral exponent*

We can now use this result to obtain the usual autocorrelation function $\rho_\Lambda(\Delta x)$ at the finest resolution (scale ratio $\Lambda > 1$, and hence the spectrum:

$$\rho_\Lambda(\Delta x) = \rho_\Lambda(1, 1, \Delta x) = \Delta x^{-K(2)} \tag{A7}$$

To obtain the spectral energy density $P(k)$:

$$P(k) = \langle |\tilde{\rho}_\Lambda(k)|^2 \rangle = \int \rho_\Lambda(x) e^{ikx} dx \tag{A8}$$

we need only use the Tauberian theorem (D = dimension of space; the above is valid for any D, even anisotropic spaces):

$$P(k) \approx k^{(D - K(2))} \tag{A9}$$

Thus, the usual (angle integrated) spectrum is

$$E(k) \approx k^{D-1} P(k) = k^{-(1 - K(2))} \tag{A10}$$

Hence, the spectral exponent is $\beta = 1 - K(2)$.

Appendix B: The lognormal multifractal

We seek moments of the form

$$\left\langle \phi_{\lambda_1}^{q_1}(\mathbf{x}_1) \phi_{\lambda_2}^{q_2}(\mathbf{x}_2) \right\rangle = e^{K(q_1, q_2)} \tag{B1}$$

Using

$$\phi_\lambda(\mathbf{x}) = \exp \Gamma_\lambda(\mathbf{x})$$

$$\Gamma_\lambda(\mathbf{x}) = \int_{A_{\lambda_1}} \exp(i\mathbf{k}\cdot\mathbf{x}) \gamma(\mathbf{k}) f(\mathbf{k}) d\mathbf{k} \tag{B2}$$

where $\gamma(\mathbf{k})$ is the subgenerator, $f(\mathbf{k})$ is the deterministic filter, $f(\mathbf{k}) = |\mathbf{k}|^{-\alpha/d}$ (see Schertzer and Lovejoy (1987) and Schertzer *et al.* (1997), α is the Levy index of the noise $\gamma(\mathbf{k})$). A_λ is the Fourier space dual of the real space zone of homogeneity. For example, if $d = 2$, and ϕ_λ is homogeneous over circular regions size λ^{-1} in real space (as we are used to), then, A_λ is the 'annulus' formed by taking a Fourier space circle radius λ with the unit circle removed.

Here, we will typically take A_λ as usual isotropic annuli, although the following will be quite general; a special case (of interest, for example, in radiative transfer) is when A_λ is a line length λ^{-1} in a given direction, centred at $\mathbf{x}$). In this case, A_λ will be an infinitely long strip in Fourier space, width λ^{-1}, oriented perpendicular to the real space line. Below, we consider the two dimensional ($d = 2$) case using $\langle \gamma(\mathbf{k}) \rangle = 0$ and $\gamma(\mathbf{k})$ is complex gaussian while noise (i.e. $\alpha = 2$) with $\langle |\gamma(\mathbf{k})|^2 \rangle = C_1 / 2\pi$. We have

$$\left\langle \phi_{\lambda_1}^{q_1}(\mathbf{x}_1) \phi_{\lambda_2}^{q_2}(\mathbf{x}_2) \right\rangle = \left\langle \exp \int_{A_{\lambda_2}} q_1 \exp(i\mathbf{k}\cdot\mathbf{x}_1) \gamma(\mathbf{k}) |\mathbf{k}|^{-1} d\mathbf{k} \right.$$

$$\left. + \int_{A_{\lambda_2}} q_2 \exp(i\mathbf{k}\cdot\mathbf{x}_2) \gamma(\mathbf{k}) |\mathbf{k}|^{-1} d\mathbf{k} \right\rangle \tag{B3}$$

To evaluate this, we divide up Fourier space into three zones:

$$A_\cap = A_{\lambda_1} \cap A_{\lambda_2}$$

$$A_{\lambda_1 - \cap} = A_{\lambda_1} - A_\cap$$

$$A_{\lambda_2 - \cap} = A_{\lambda_2} - A_\cap \tag{B4}$$

In each zone, we will apply the standard results for addition of second characteristic functions:[35]

$$\frac{2\pi}{C_1}\log\langle\phi_{\lambda_1}^{q_1}(\mathbf{x}_1)\phi_{\lambda_2}^{q_2}(\mathbf{x}_2)\rangle = \int_{A_{\lambda_1}\cap} |q_1\ \exp(i\mathbf{k}\cdot\mathbf{x}_1)|^2\,|\mathbf{k}|^{-2}\mathrm{d}\mathbf{k} + \int_{A_{\lambda_2}\cap} |q_2\ \exp(i\mathbf{k}\cdot\mathbf{x}_2)|^2|\mathbf{k}|^{-2}\mathrm{d}\mathbf{k}$$
$$+ \int_{A\cap} |q_1\ \exp(i\mathbf{k}\cdot\mathbf{x}_1) + q_2\ \exp(i\mathbf{k}\cdot\mathbf{x}_2)|^2\,|\mathbf{k}|^{-2}\mathrm{d}\mathbf{k} \tag{B5}$$

We finally obtain, using $\Delta\mathbf{x} = (\mathbf{x}_1 - \mathbf{x}_2)$:

$$\frac{2\pi}{C_1}\log\langle\phi_{\lambda_1}^{q_1}(\mathbf{x}_1)\phi_{\lambda_2}^{q_2}(\mathbf{x}_2)\rangle = q_1^2 \int_{A_{\lambda_1}} |\mathbf{k}|^{-2}\mathrm{d}\mathbf{k}$$
$$+ q_2^2 \int_{A_{\lambda_2}} |\mathbf{k}|^{-2}\mathrm{d}\mathbf{k} + 2q_1q_2 \int_{A\cap} \cos(\mathbf{k}\cdot\mathbf{x})|\mathbf{k}|^{-2}\mathrm{d}\mathbf{k} \tag{B6}$$

Therefore, we define the correlation as

$$\varphi = \frac{\int_{A\cap} \cos(\mathbf{k}\cdot\Delta\mathbf{x})|\mathbf{k}|^{-2}\mathrm{d}\mathbf{k}}{2\pi(\xi_1\,\xi_2)^{1/2}} \tag{B7}$$

where

$$\xi_i = \frac{1}{2\pi}\int_{A_{\lambda_i}} |\mathbf{k}|^{-2}\mathrm{d}\mathbf{k} \tag{B8}$$

It is not hard to show that $\varphi \leqslant \max[(\xi_1/\xi_2)^{1/2}, (\xi_2/\xi_1)^{1/2}]$. In the special case of interest here, A_{λ_1}, A_{λ_2} are concentric annuli with inner radius 1, outer radius λ_1, λ_2, we have $\mathrm{d}k = 2\pi|\mathbf{k}|\mathrm{d}|\mathbf{k}|$ hence $\xi_i = \log\lambda_i$, and A_λ is equal to the smaller annulus so that when $\Delta x = 0$, we obtain the simplification indicated in equation 16.

We have

$$\log\langle\phi_{\lambda_1}^{q_1}(\mathbf{x}_1)\phi_{\lambda_2}^{q_2}(\mathbf{x}_2)\rangle = K(q_1, q_2) = C_1 q_1^2\,\xi_1 + C_1 q_2^2\,\xi_2$$
$$+ 2C_1 q_1 q_2\,\varphi(\xi_1\,\xi_2)^{1/2} \tag{B9}$$

corresponding to a normalized, conservative ϕ: (i.e. $\langle\phi_{\lambda_1}\rangle = \langle\phi_{\lambda_2}\rangle = 1$).

To obtain a normalised K, we subtract

$$K \to K(q_1, q_2) - q_1 K(1, 0) - q_2 K(0, 1) \tag{B10}$$

The normalised K is thus

$$K(q_1, q_2) = C_1(q_1^2 - q_1)\xi_1 + C_1(q_2^2 - q_2)\xi_2 + 2C_1 q_1 q_2\,\varphi(\xi_1\,\xi_2)^{1/2} \tag{B11}$$

[35] i.e. for any complex w, $\langle e^{w\gamma}\rangle = e^{(|w|^2\sigma^2)/2}$ where $\sigma^2 = \langle|\gamma|^2\rangle$, γ is a complex gaussian random variable with independent phase and modulus.

which, for lognormal multifractals, is slightly more general than the result of appendix A (the latter result is valid for any multifractal with $\lambda_1 = \lambda_2$).

Appendix C: Autocorrelations and spectra conditional on presence of a singularity order γ_m

We first seek the cross-moments at points $\mathbf{x}_1, \mathbf{x}_2$ conditional on the measurement of value at point $\mathbf{x}$ (all values are at resolution λ). The goal is to calculate the bias introduced by the conditioning in the statistics of satellite imagery at scale $\lambda_s < \lambda_m$. Using the notation of appendix B, we can define the conditional two-point statistics:

$$\left\langle \phi^{q_1}_{\lambda_m}(\mathbf{x}_1)\phi^{q_2}_{\lambda_m}(\mathbf{x}_2) | \gamma_m(\mathbf{x}) \right\rangle = \lambda_m^{K(q_1, q_2 | \gamma_m)} \tag{C1}$$

where all values are measured at scale λ_m.

This is the conditional cross-moment conditioned on a singularity order γ_m existing at point $\mathbf{x}$. Now, the conditional moments can be expressed in terms of the Legendre transform of the three-point moment exponent $K(q_1, q, q_m)$ with respect to q_m:

$$K(q_1, q_2 | \gamma_m) = K(q_1, q_2, \gamma_m) - K(0, 0, \gamma_m) \tag{C2}$$

Using the form for the lognormal multifractal, one obtains explicitly

$$K(q_1, q_2 | \gamma_m) = K(q_1, q_2) + (\gamma_m + C_1)(q_1 \varphi_{1m} + q_2 \varphi_{2m}) - C_1(q_1 \varphi_{1m} + q_2 \varphi_{2m})^2 \tag{C3}$$

This reduces to the corresponding two-point exponent as expected when q_2 or $q_1 = 0$. This conditional moment exponent can be conveniently rewritten

$$K(q_1, q_2 | \gamma_m) = K(q_1, q_2) + \gamma_m Q - K(Q)$$
$$Q = q_1 \varphi_{1m} + q_2 \varphi_{2m} \tag{C4}$$

C.1. *Spatially averaged autocorrelation and the spectrum*

In order to calculate the conditional spectrum, we must calculate the autocorrelation with the coordinate $\mathbf{x}$ fixed (in the case of satellite pictures, somewhere in the satellite image region $\lambda_s^{-1} X \lambda_s^{-1}$) and average the result over all $\mathbf{x}_{\text{lag}}$ with $\mathbf{x}_1 = \mathbf{x}_{\text{lag}}$, $\mathbf{x}_2 = \mathbf{x}_{\text{lag}} + \Delta\mathbf{x}$ and $\Delta\mathbf{x}$ fixed (see figure 8(*e*)). Once again, we will exploit the saddle point method; the integration in this averaging will yield $\lambda_m^{K(q_1, q_2 | \gamma_m)_{ave}}$ with

$$K(q_1, q_2 | \gamma_m)_{ave} = K(q_1, q_2) + \max_{Q_{\min} < Q < Q_{\max}}(\gamma_m Q - K(Q)) \tag{C5}$$

with Q given by equation (C4); the maximum in the Legendre transform (C5) is over all the allowed values of Q with $Q_{\min}$, $Q_{\max}$ constrained by the geometrical restrictions on $\varphi(|\mathbf{x} - \mathbf{x}_{\text{lag}}|)$, $\varphi(|\mathbf{x} - \mathbf{x}_{\text{lag}} - \Delta\mathbf{x}|)$.

Consider the special case $q_1 = q_2 = q$. In this case, for $\Delta\mathbf{x} > \lambda_m^{-1}$ (see equation (20)) and $\lambda_s^{-1} - \Delta\mathbf{x} > \lambda_m^{-1}$ (due to the restriction $\varphi < 1$),

$$Q = -q \frac{\log(|\mathbf{x} - \mathbf{x}_{\text{lag}}||\mathbf{x} - \mathbf{x}_{\text{lag}} - \Delta\mathbf{x}|)}{\log \lambda_m} \tag{C6}$$

If we now assume that $\mathbf{x}$, $\mathbf{x}_{\text{lag}}$ are somewhere within an interval size λ_s^{-1}, we can show that, to within unimportant factors of order 1, for all $\mathbf{x}$, $\mathbf{x}_{\text{lag}}$, ($\Delta\mathbf{x}$ fixed), the distance product is bounded by

$$\lambda_m^{-1} \Delta\mathbf{x} < |\mathbf{x} - \mathbf{x}_{\text{lag}}||\mathbf{x} - \mathbf{x}_{\text{lag}} - \Delta\mathbf{x}| < \lambda_s^{-2} \tag{C7}$$

Taking logs and dividing through by log λ_m, we therefore obtain (ignoring the constant of order 1)

$$1+\varphi > Q/q > 2\zeta; \quad \zeta = \frac{\log \lambda_s}{\log \lambda_m} \tag{C8}$$

i.e. for $\Delta\mathbf{x}$ fixed, we have upper and lower bounds on Q: $Q_{\max} \approx q(1+\varphi)$, $Q_{\min} \approx 2q\zeta$. The exponent of the conditional autocorrelation function integrating over $\mathbf{x}_{\text{lag}}$ is thus obtaining from the Legendre transform with Q bounded as indicated.

Note also that, since

$$1 \geqslant \varphi \geqslant \zeta \tag{C9}$$

we have the following bounds on $Q_{\max}$ as we vary $\Delta\mathbf{x}$ from 1 pixel ($\max(Q_{\max})$) to the entire image ($\min(Q_{\max})$):

$$\begin{aligned} \min_{\Delta x}(Q_{\max}) &\approx q(1+\zeta) \\ \max_{\Delta x}(Q_{\max}) &\approx 2q \end{aligned} \tag{C10}$$

For $q=1$, we have the following three cases depending on the value of the critical moment Q_m corresponding to the conditioning singularity: $\gamma_m = K'(Q_m)$ or equivalently $c'(\gamma_m) = Q_m = (\gamma_m/C_1 + 1)/2$.

C.2.1. $Q_m > \max_{\Delta x}(Q_{\max})$, i.e. $\gamma_m > 3C_1$

In this case, the Legendre achieves its maximum at $Q_{\max} = 1+\varphi$ and, furthermore, this maximum will be valid over the entire range of $\Delta\mathbf{x}$. We therefore obtain

$$\overline{\langle \phi_{\lambda_m}(\mathbf{x}_{\text{lag}}) \phi_{\lambda_m}(\mathbf{x}_{\text{lag}} + \Delta\mathbf{x}) | \gamma_m(\mathbf{x}) \rangle} = \lambda_m^{(C_1+\gamma_m)\phi} \lambda_m^{-C_1\varphi^2} \lambda_m^{\gamma_m} \approx \Delta\mathbf{x}^{C_1\zeta - \gamma_m} \tag{C11}$$

where the overbar indicates spatial averaging over all $\mathbf{x}_{\text{lag}}$. The approximtion on the far right was obtained by linearising the (quadratic) φ dependent part about the mean value $\varphi = (1+\zeta)/2$. The spectral exponent β is now obtained in the usual way (section A.2), yielding

$$\beta = 1 - \gamma_m + C_1\zeta \tag{C12}$$

If we compare this to the usual unconditioned spectral exponent ($\beta = 1 - 2C_1$), we see that the effect of conditioning is to flatten the spectrum by $2\Delta H$, i.e. with fractional integration order ΔH:

$$\Delta H = C_1\left(1 + \frac{\zeta}{2}\right) - \frac{\gamma_m}{2} \tag{C13}$$

Since this result is valid for $\gamma_m > 3C_1$, we find

$$\Delta H < -\frac{C_1}{2}(1-\zeta) \tag{C14}$$

since $\lambda_s < \lambda_m$, $\zeta < 1$, and hence this is < 0 (corresponding to a fractional differentiation), indicating that the effect of this conditioning is indeed to flatten the spectrum.

Interpretation. This corresponds to the low-resolution situation, in which a 'hot spot' is of the order of single pixel. In that case, the spectrum is considerably flattened by the presence of the hot spot. On the contrary, a blow-up around the hot spot, such that virtually the entire picture is 'hot', will give smooth variations corresponding roughly to the unconditional statistics.

C.2.2. $\min_{\Delta x}(Q_{\max}) < Q_m < \max_{\Delta x}(Q_{\max})$, i.e. $C_1(2Q_{\min}) < \gamma_m < 3C_1$

In this range, there will be a critical φ (and hence distance) where the Legendre maximum is no longer attained at the maximum value $Q_{\max} = 1 + \varphi$, but rather at Q_m. The critical value is obtained at the critical distance Δx_{cr}, such that

$$\varphi_{cr} = \varphi(\Delta x_{cr}) = \frac{1}{2}\left(\frac{\gamma_m}{C_1} - 1\right) \tag{C15}$$

Starting at the small scale, for $\Delta x < \Delta x_{cr}$, we have $\varphi > \varphi_{cr}$, and we have the same result as before. At larger distances, the Legendre transform gives an exponent $c(\gamma_m)$, which is independent of Δx, so that (due to the $K(1, 1)$ term), we recover the usual slope ($\beta = 1 - 2C_1$). At still lower frequencies, the prefactor changes (the Legendre transform gives $\gamma_m Q_{\min} - K(Q_{\min})$), but we have the same dependence of φ and hence Δx (only the standard $K(1,1)$ term remains). This is the regime where the conditioning breaks the scaling.

C.2.3. $Q_m < \min_{\Delta x}(Q_{\max})$, i.e. $\gamma_m < (C_1(2Q_{\min})$

In this case, there is no more φ dependence (except via $K(1,1)$), so that, although (when $Q_m > Q_{\min}$), the value of the autocorrelation function may be different from the standard value, we obtain the standard scaling exponent throughout.

C.3. *The interpretation of the conditional autocorrelation/conditional spectrum*

We have calculated the spatially averaged correlation conditional on there being a singularity γ_m at location **x**. This means that, if we had an infinite ensemble of realisations each with such a singulariity at *exactly the same location* **x** and averaged over all of them, we would obtain the anomalous behaviour indicated. However, in actual fact, we are more often interested in inferring the behaviour of the spatially averaged autocorrelation function/spectrum on individual realisations. In this case, we must have an idea of the dispersion about the mean behaviour: if the dispersion is large enough, then we will be unlikely to be able to identify the corresponding systematic behaviour compared to the background 'noise'. By calculating the relative RMS conditional autocorrelation (i.e. by considering the case $q_1 = q_2 = q = 2$ in the above), we can show that indeed the effect of the singularity will likely only be pronounced on a single realisation for fairly large γ_m. Rather than giving the analytic results, we show some simple numerics illustrating the very large dispersions obtained, figure C1 shows that the relative dispersion increases rapidly as γ_m decreases.

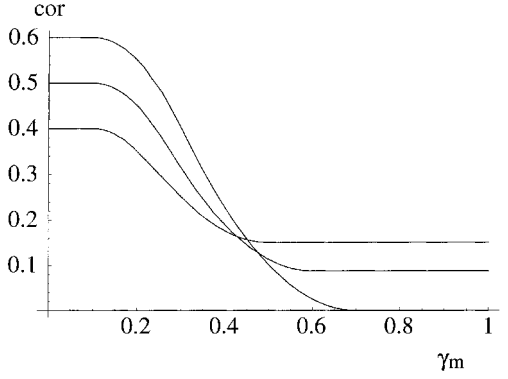

Figure C1. This shows the relative RMS exponent R (labelled 'cor') for distances Δx corresponding to $\varphi(\Delta x) = 0.5, 0.75, 1$ (bottom to top at left corresponding to the largest scale, and intermediate scale and 1 pixel scale, respectively), with parameters $C_1 = 0.1$ and $\lambda = \lambda_s^2$ (i.e. $Q_{\min} = 1$). Since the actual relative RMS factor is λ^R, if $\lambda = 10^6$ (as would be the case for 10m resolution data: 10^4 km/10 m $= 10^6$), for γ_m less than about 0.5, the dispersion factor is enormous. However, for large γ_m, the effect of the conditioning should be visible on single realisations.

Acknowledgments

The authors thank E. Bourget of Laval University and A. Thomas of the Atlantic Centre for Remote Sensing for supplying the MIES data and A. Bambridge for much of the data analysis. They also acknowledge partial financial support from the Coastal Heterogeneity and Scaling Experiment (NSERC, Canada).

References

Ait-Kheddache, A., and Rajala, S., 1988, Texture classification based on higher-order fractals. *ICASSP International Conference on Acoustics, Speech and Signal Processing*, New York, pp. 1112–1115.

Bak, P., Tang, C., and Weiessenfeld, K., 1987, Self-organized criticality: an explanation of 1/f noise. *Physical Review Letter*, **59**, 381–384.

Bak, P., Tang, C., and Weiessenfeld, K., 1988, Self-organized criticality. *Physical Review Letters*, **A 38**, 364–374.

Barale, V., and Schlittenhardt, P. M., 1993, *Ocean colour: theory and applications in a decade of CZCS Experience*. (Dordrecht: Kluwer).

Bian, L., 1997, Multiscale nature of spatial data in scaling up environmental models. In *Scaling in Remote Sensing and Geographical Information Systems*, edited by M. G. D. Quattrochi (Boca Raton, Florida: Lewis), pp. 13–26.

Bourissou, A., Pham, K., and Lèvy-Vehel, J., 1994, A multifractal approach for terrain characterization and classification on SAR images. *Proceedings of the IGARSS 94, Pasadena, September* (IEEE).

Brax, P., and Pechanski, R., 1991, Levy stable law description on intermittent behaviour and quark-gluon phase transitions. *Physics Letters B*, **353**, 225–230.

Chou, Y. H., 1991, Map resolution and spatial autocorrelation. *Geographic Analysis*, **23**, 228.

Claeredeboudt, M., Lovejoy, S., Tessier, Y., Currie, J., Roff, J., Bourget, E., and Schertzer, D., 1999, Universal multifractals and ocean patchiness: a new framework, in preparation.

Clarke, W., and Avery, K., 1976, The effects of data aggregation in statistical analysis. *Geogr. Anal.*, **8**, 428.

Cracknell, A. P., 1998, Synergy in remote sensing — what's in a pixel? *International Journal of Remote Sensing*, **19**, 2025–2047.

Datcu, M., and Seidel, K., 1995, Fractal and multi-resolution techniques for the understanding of geoinformation. In *Fractals in Geoscience and Remote Sensing*, edited by G. G. Wilkinson, I. Kanellopoulos and J. Mégier (Brussels: Official Publications of the European Communities), pp. 56–84.

Davis, A., Lovejoy, S., Gabriel, P., Schertzer, D., and Austin, G. L., 1990, Discrete angle radiative transfer. Part III: Numerical results on homogeneous and fractal clouds. *Journal of Geophysical Research*, **95**, 11729–11742.

Davis, A., Lovejoy, S., and Schertzer, D., 1993, Supercomputer simulation of radiative transfer inside multifractal cloud models. *International Radiation Symposium 92 Tallinn, 3–8 August 1992* (Hampton, VA: Deepak).

Davis, A., Marshak, A., Wiscombe, W., and Cahalan, R., 1996, Scale invariance of liquid water distributions in marine stratocumulus. Part I: Spectral properties and stationarity issues. *Journal of Atmosphere Science*, **53**, 1538–1558.

de Jong, S., 1995, Mapping spatial variability in landscapes: an example using fractal dimensions. In *Fractals in Geoscience and Remote Sensing*, edited by G. G. Wilkinson, I. Kanellopoulos and J. Mégier (Brussels: Official Publications of the European Communities), pp. 176–210.

Denman, K. L., and Platt, T., 1975, The variance spectrum of phytoplankton in a turbulent ocean. *Journal of Marine Research*, **34**, 593–601.

Deuman, K. L., Okubo, A., and Platt, T., 1976, The chlorophyll fluctuation spectrum in the sea. *Limnology and Oceanography*, **22**, 1033–1038.

Falco, T., Francis, F., Lovejoy, S., Schertzer, D., Kerman, B., and Drinkwater, M., 1996, Scale invariance and universal multifractals in sea ice synthetic aperature radar reflectivity fields. *IEEE Transactions in Geoscience and Remote Sensing*, **34**, 906–914.

Fisher, P., 1997, The pixel: a snare and a delusion. *International Journal of Remote Sensing*, **18**, 679–685.

Frisch, U., Sulem, P. L., and Nelkin, M., 1978, A simple dynamical model of intermittency in fully develop turbulence. *Journal of Fluid Mechanics*, **87**, 719–724.

Gabriel, P., Lovejoy, S., Schertzer, D., and Austin, G. L., 1988, Multifractal analysis of resolution dependence in satellite imagery. *Geophysical Research Letters*, **15**, 1373–1376.

Gabriel, P., Lovejoy, S., Davis, A., Schertzer, D., and Austin, G. L., 1990, Discrete angle radiative transfer. Part II: Renormalization approach to scaling clouds. *Journal of Geophysical Research*, **95**, 11717–11728.

Gaonac'h, H., Lovejoy, S., and Schertzer, D., 2000, Multifractal analysis of infrared imagery of active thermal features at Kilauea volcano. *Journal of Geophyical Research*, submitted.

Gonzalez, R. C., and Wintz, P., 1987, *Digital Image Processing* (Menlo Park, California: Addision-Wesley).

Harvey, D. A., Gaonac'h, H., Lovejoy, S., and Schertzer, D., 2000, Multifractal characterization of remotely sensed volcanic features: a case study from Kiluaea volcano, Hawaii. *Fractals*, in press.

Keller, J. M., Chen, S., and Crownover, R. M., 1989, Texture description and segmentation through fractal geometry. *Computer Graphics and Image Processing*, **45**, 150–166.

Kida, S., 1991, Log stable distribution and intermittency of turbulence. *Journal of the Physical Society of Japan*, **60**, 5–8.

Kuklinski, W. S., 1994, Utilization of fractal image models in medical image processing. *Fractals*, **2**, 363–369.

Laferrière, A., and Gaonac'h, H., 1999, Multifractal properties of visible reflectance fields from basaltic volcanoes. *Journal of Geophysical Research*, **104**, 5115–5126.

Lavallée, D., 1991, Multifractal techniques: analysis and simulation of turbulent fields. McGill University, Montréal.

Lavallée, D., Jourdan, D., Gautier, C., and Hooge, C., 1993a, Universal multifractal properties of microwave satellite data. *ASPRS/ACSM, Annual Convention, May, New Orleans* (Hampton, VA: Deepak), pp. 121–125.

Lavallée, D., Lovejoy, S., Schertzer, D., and Ladoy, P., 1993b, Nonlinear variability and landscape topography: analysis and simulation. In *Fractals in Geography*, edited by L. De Cola and N. Lam (New York: Prentice-Hall), pp. 171–205.

Lévy-Véhel, J., 1995, Multifractal analysis of remotely sensed images. In *Fractals in Geoscience and Remote Sensing*, edited by G. G. Wilkinson, I. Kanellopoulos and J. Mégier (Brussels: Official Publications of the European Communities), pp. 85–106.

Lévy-Véhel, J., and Berroir, J.-P., 1994 Image analysis through multifractal description. In *Fractals in the Natural and Applied Sciences*, edited by M. Novak (North-Holland: Elsevier), pp. 261–274.

Lévy-Véhel, J., and Mignot, P., 1994, Multifractal segmentation of images. *Fractals*, **2**, 371–377.

Lewis, G., Lovejoy, S., Schertzer, D., and Pecknold, S., 1999, The scale invariant generator technique for parameter estimates in generalized scale invariance. *Computers and Geosciences*, **25**, 963–978.

Lovejoy, S., and Schertzer, D., 1985, Generalized scale invariance and fractal models of rain. *Water Resources Research*, **21**, 1233–1250.

Lovejoy, S., and Schertzer, D., 1988, Extreme Variability, Scaling and fracals in remote sensing: analysis and simulation. In *Digital Image Processing in Remote Sensing*, edited by P. J. Muller (London: Taylor and Francis) pp. 177–212.

Lovejoy, S., and Schertzer, D., 1990, Multifractals, universality classes and satellite and radar measurements of cloud and rain fields. *Journal of Geophysical Research*, **95**, 2021.

Lovejoy, S., and Schertzer, D., 1991, Multifractal analysis techniques and the rain and clouds fields from 10^{-3} to 10^{6} m. In *Non-linear Variability in Geophysics: Scaling and Fractals*, edited by D. Schertzer and S. Lovejoy, (Dordrecht: Kluwer), pp. 111–144.

Lovejoy, S., and Schertzer, D., 1993, Multifractals and resolution dependence of remotely sensed data. *16th Canadian symp. on remote sensing/8ieme congrès de l'Assoc. Qué. Télé, 6–10 June 1993, Sherbrooke, Quebec* (Ottawa: Canadian Remote Sensing Society), pp. 775–780.

Lovejoy, S., and Schertzer, D., 1995, How bright is the coast of Brittany? In *Fractals in Geoscience and Remote Sensing*, edited by G. Wilkinson (Luxembourg: Office for Official Publications of the European Communities), pp. 102–151.

Lovejoy, S., Schertzer, D., and Tsonis, A. A., 1987, Functional box-counting and multiple dimensions in rain. *Science*, **235**, 1036–1038.

Lovejoy, S., Gabriel, P., Davis, A., Schertzer, D., and Austin, G. L., 1990, Discrete angle radiative transfer. Part I: Scaling and similarity, universality and diffusion. *Journal of Geophysical Research*, **95**, 11699–11715.

Lovejoy, S., Schertzer, D., Silas, P., Tessier, Y., and Lavallée, D., 1993, The unified scaling model of atmospheric dynamics and systematic analysis in cloud radiances. *Annales Geophysicae*, **11**, 119–127.

Lovejoy, S., Watson, B., Schertzer, D., and Brosamleu, G., 1995, Scattering in multifractal media. In *Particle Transport in Stochastic Media*, edited by L. Briggs (Portland, Oregon: American Nuclear Society), pp. 750–760.

Lovejoy, S., Duncan, M., and Schertzer, D., 1996, The scalar multifractal radar observer's problem. *Journal of Geophysical Research*, **31D**, 26479–26492.

Lovejoy, S., Schertzer, D., Stanway, J. D., Watson, B., and Sachs, D., 1997, Multifractal modelling and analysis of radiation in clouds: 5000km to 50cm. *Proceedings of 7th Atmos. Rad. Meas. (ARM) Meeting, March, San Antonio* (Washington: US Department of Energy).

Lovejoy, S., Currie, W. J. C., Tessier, Y., Claeredeboudt, M., Bourget, E., Roff, J., and Schertzer, D., 2000, Universal multfractals and ocean patchiness: phyto-plankton, physical fields and coastal heterogeneity. *Journal of Plankton Research*, in press.

Mandelbrot, B. B., 1967, How long is the coastline of Britain? Statistical self-similarity and fractional dimension. *Science*, **155**, 636–638.

Mandelbrot, B. B., 1974, Intermittent turbulence in self-similar cascades: divergence of high moments and dimension of the carrier. *Journal of Fluid Mechanics*, **62**, 331–350.

Marceau, D. J., Gratton, D. J., Fournier, R. A., and Fortin, J.-P., 1994a, Remote sensing and the measurement of geographical entities in a forested environment. 2. The optimal spatial resolution *Remote Sensing of Environment*, **49**, 105–117.

Marceau, D. J., Howarth, P. J., and Gratton, D. J., 1994b, Remote sensing and the measurement of geographical entities in a forested environment. 1. The scale and spatial aggregation problem. *Remote Sensing of Environment*, **49**, 93–104.

Marsan, D., Schertzer, D., and Lovejoy, S., 1996, Causal space-time multifractal processes: predictability and forecasting of rain fields. *Journal Geophysical Research*, **31**, 26 333–26 346.

Martinez, P., 1998, Analyse de texture appliquée à l'étude des images SAR: apport des techniques multifractals, PGD thesis, Université Pierre et Marie Curie, Paris, France.

Mignot, P., Lèvy-Vèhel, J., and Lechevallier, Y., 1992, Arthur: un systëme dĭanalyse de texture. *Traitement du Signal*, **9**, 507–517.

Monin, A. S., and Yaglom, A. M., 1975, *Statistical Fluid Mechanics* (Boston, Massachusetts: MIT Press).

Mussigman, U., 1990, Texture analysis using fractal dimensions. In *Fractal Geometry and Computer Graphics*, edited by J. L. Encarnacao, H. O. Peitgen, G. Sakas and G. Englert (Berlin: Springer Verlag), pp. 217–230.

Naud, C., Schertzer, D., and Lovejoy, S., 1996, Fractional integration and radiative transfer in multifractal atmospheres. In *Stochastic Models in Geosystems*, edited by W. Woyczynski, and S. Molchansov (New York: Springer-Verlag), pp. 239–267.

Novikov, E. A., and Stewart, R., 1964, Intermittency of turbulence and spectrum of fluctuations in energy-disspation. *Izvestia Akademia Nauk SSSR Serie Geofizik*, **3**, 408–412.

Openshaw, S., 1984, *The Modified Areal Unit Problem* (Norwich, UK: Geobooks).

Parisi, G., and Frisch, U., 1985, A multifractal model of intermittency. In *Turbulence and Predictability in Geophysical Fluid Dynamics and Climate Dynamics*, edited by M. Ghil, R. Benzi and G. Parisi (Amsterdam: North Holland), pp. 84–88.

Pascual, M., Ascioti, A., and Caswell, H., 1995, Intermittency in the plankton: a multifractal analysis of zooplankton biomas variability. *Journal of Plankton Research*, **17**, 1209–1232.

Pecknold, S., Lovejoy, S., Schertzer, D., Hooge, C., and Malouin, J. F., 1993, The simulation of universal multifractals. In *Cellular Automata: prospects in astronomy and astrophysics*, edited by J. M. Perdang and A. Lejeune (Singapore: World Scientific), pp. 228–267.

Pecknold, S., Lovejoy, S., and Schertzer, D., 2000, Stratified multifratal magnetization and surface geometric fields, part 2: multifractal analysis and simulation. *Geophys. Inter. J.*, in press.

Peleg, S., Naor, J., Hartley, R., and Avnir, D., 1984, Multiple resolution texture analysis and classification. *IEEE, PAMI*, **6**, 518–523.

Pentland, A., 1984, Fractal based description of natural scenes. *IEEE Trans. on PAMI*, **6**, 661–674.

Perrin, J., 1913, *Les Atomes* (Paris: NRF-Gallimard).

Pflug, K., Lovejoy, S., and Schertzer, D., 1993, Generalized scale invariance, differential rotation and cloud texture. *Journal of Atmospheric Sciences*, **50**, 538–553.

Platt, T., 1978, Spectral analysis of spatial structure in phytoplankton populations. In *Spatial Pattern in Plankton Communities*, edited by J. H. Steele (New York: Plenum Press), pp. 73–85.

Platt, T., and Denman, K. L., 1975, Spectral analysis in ecology. *Annual Review of Ecological Systems*, **6**, 189–210.

Raffy, M., 1994 a, Change of scale theory: a capital challenge for space observation of earth. *International Journal of Remote Sensing*, **15**, 2353–2357.

Raffy, M., 1994 b, The role of spatial resolution in quantification problems: spatialization method. *International Journal of Remote Sensing*, **15**, 2381–2392.

Rees, W. G., 1995, Characterization of imaging of fractal topography. In *Fractals in Geoscience and Remote Sensing*, edited by G. Wilkinson (Luxembourg: Office for Official Publications of the European Communities), pp. 298–325.

Richardson, L. F., 1961, The problem of contiguity: an appendix of statistics of deadly quarrels. *General Systems Yearbook*, **6**, 139–187.

Sachs, D., Lovejoy, S., and Schertzer, D., 1999, The multifractal scaling of cloud radiances from 1 m to 1 km. *Fractals*, in press.

Salvadori, G., 1993, Multifracttali stocastici: theoria e applicazioni. PhD thesis, Universita di Milano, Milan, Italy.

Salvadori, G., Ratti, S., Belli, G., Lovejoy, S., and Schertzer, D., 1993, Multifractal and Fourier analysis of Seveso pollution. *J. of Toxicological and Environ. Chem.*, **43**, 63–76.

Salvadori, G., Schertzer, D., and Lovejoy, S., 1999, Multifractal objective analysis and interpolation. *Stochastic Environmental Research and Risk Analysis*, in press.

Schertzer, D., and Lovejoy, S., 1985, Generalised scale invariance in turbulent phenomena. *Physico-Chemical Hydrodynamics Journal*, **6**, 623–635.

Schertzer, D., and Lovejoy, S., 1987, Physical modeling and analysis of rain and clouds by anisotropic scaling of multiplicative processes. *Journal of Geophysical Research*, **92**, 9693–9714.

Schertzer, D., and Lovejoy, S., 1989a, Generalized scale invariance and multiplicative processes in the atmosphere. *Pageoph*, **130**, 57–81.

Schertzer, D., and Lovejoy, S., 1989b, Nonlinear variability in geophysics: multifractal analysis and simulation. In *Fractals: physical origin and consequences*, edited by L. Pietronero (New York: Plenum), 49–63.

Schertzer, D., and Lovejoy, S., 1994, Multifractal generation of self-organized criticality. In *Fractals In the Natural and Applied Sciences*, edited by M. M. Novak (North-Holland: Elsevier), pp. 325–339.

Schertzer, D., and Lovejoy, S., 1995, From scalar cascades to Lie cascades: joint multifractal analysis of rain and cloud processes. In *Space/Time Variability and Interdependance for Various Hydrological Processes*, edited by R. A. Feddes, (New York: Cambridge University Press), pp. 153–173.

Schertzer, D., and Lovejoy, S., 1997, Universal multifractals do exist! *J. Appl. Meteor.*, **36**, 1296–1303.

Schertzer, D., Lovejoy, S., Lavallée, D., and Schmitt, F., 1991, Universal hard multifractal turbulence: theory and observation. In *Nonlinear Dynamics of Structures*, edited by R. Z. Sagdeev, U. Frisch, A. S. Moiseev and A. Erokhin (Singapore: World Scientific), pp. 213–235.

Schertzer, D., Lovejoy, S., and Schmitt, F., 1995, Structures in turbulence and multifractal universality. In *Small-Scale Structures in 3D and MHD Turbulence*, edited by M. Meneguzzi, A. Pouquet, and P. L. Sulem (New York: Springer-Verlag), pp. 137–144.

Schertzer, D., Lovejoy, S., Schmitt, F., Chigirinskaya, Y., and Marsan, D., 1997, Multifractal cascade dynamics and turbulent intermittency. *Fractals*, **5**, 427–471.

Schmitt, F., Schertzer, D., Lovejoy, S., and Marchal, P., 1997, Multifractal analysis of satellite images: towards an automatic segmentation. In *Fractals in Engineering* (Arcachon: Jules), pp. 103–109.

Schuster, H. G., 1988, *Deterministic Chaos* (New York: VCH).

Seuront, L., Schmitt, F., Schertzer, D., Lagadeuc, Y., and Lovejoy, S., 1996a, Multifractal analysis of Eulerian and Lagrangian variability of physical and biological fields in the ocean. *Nonlinear Processes in Geophysics*, **3**, 236–246.

Seuront, L., Schmitt, F., Lagadeuc, Y., Schertzer, D., Lovejoy, S., and Frontier, S., 1996b, Universal multifractal structure of phytoplankton biomass and temperature in the ocean. *Geophysical Research Letters*, **23**, 3591–3594.

She, Z., S., and Levesque, E., 1994, *Physical Review Letters*, **72**, 336–339.

Stanway, J. D., 2000, Multifractal analysis of cloud radiances from 5000km to 1km. MSc thesis, McGill University, Montréal.

Sturm, B., 1993, CZCS data processing algorithms. In *Ocean Colour: yheory and applications in a decade of CZCS experience*, edited by V. Barale and P. M. Schlittenhardt (Dordrecht: Kluwer Academic Press), pp. 95–116.

Tessier, Y., 1993, Multifractal objective analysis, rain and clouds. PhD thesis, McGill University, Montréal.

Tessier, Y., Lovejoy, S., Schertzer, D., Lavallée, D., and Kerman, B., 1993, Universal multifractal indices for the ocean surface at far red wavelengths. *Geophysical Research Letters*, **20**, 1167–1170.

Tessier, Y., Lovejoy, S., and Schertzer, D., 1994, The Multifractal Global Raingage Network: Analysis and simulation. *Journal of Applied Meteorology*, **32**, 1572–1586.

Verge, M., and Souriau, M., 1994, A multi-scale analysis of continental relief in Southern Franc. *International Journal of Remote Sensing*, **15**, 2409–2419.